

Chemical Dynamics Study on the Gas-Phase Reaction of the D1-Silyldyne Radical (SiD; X²Π) with Deuterium Sulfide (D₂S) and Hydrogen Sulfide (H₂S)

Shane J. Goettl,^a Srinivas Doddipatla,^a Zhenghai Yang,^a Chao He,^a Ralf I. Kaiser^{a,*}

^a *Department of Chemistry, University of Hawai'i at Manoa, Honolulu, Hawaii 96822, USA*

Corresponding Author: ralfk@hawaii.edu

Mateus Xavier Silva,^b Breno R. L. Galvão^{b,*}

^b *Centro Federal de Educação Tecnológica de Minas Gerais, CEFET-MG, Av. Amazonas 5253, 30421-169 Belo Horizonte, Minas Gerais, Brazil*

Corresponding Author: brenogalvao@gmail.com

Tom J. Millar^{c,*}

^c *School of Maths and Physics, Queen's University Belfast, University Road, Belfast BT7 1NN, Northern Ireland*

Corresponding Author: Tom.Millar@qub.ac.uk

ABSTRACT

The reactions of the D1-silyldiyne radical (SiD ; $X^2\Pi$) with deuterium sulfide (D_2S ; X^1A_1) and hydrogen sulfide (H_2S ; X^1A_1) were conducted utilizing a crossed molecular beams machine under single collision conditions. The experimental work was carried out in conjunction with electronic structure calculations. The elementary reaction commences with a barrierless addition of the D1-silyldiyne radical to one of the non-bonding electron pairs of the sulfur atom of hydrogen (deuterium) sulfide followed by possible bond rotation isomerization and multiple atomic hydrogen (deuterium) migrations. Unimolecular decomposition of the reaction intermediates lead eventually to the D1-thiosilaformyl radical (DSiS) (**p1**) and D2-silanethione (D_2SiS) (**p3**) via molecular and atomic deuterium loss channels ($\text{SiD}-\text{D}_2\text{S}$ system) along with the D1-thiosilaformyl radical (DSiS) (**p1**) and D1-silanethione (HDSiS) (**p3**) through molecular and atomic hydrogen ejection ($\text{SiD}-\text{H}_2\text{S}$ system) via indirect scattering dynamics in barrierless and overall exoergic reactions. Our study provides a look into the complex dynamics of the silicon and sulfur chemistries involving multiple deuterium/hydrogen shifts and tight exit transition states, as well as insight into silicon- and sulfur-containing molecule formation pathways in deep space. Although neither of the non-deuterated species – the thiosilaformyl radical (HSiS) and silanethione (H_2SiS) – have been observed in the interstellar medium (ISM) thus far, astrochemical models presented here predict relative abundances in the Orion Kleinmann-Low nebula to be sufficiently high enough for detection.

1. Introduction

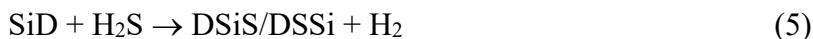
Ever since Langmuir devised the notion of isovalency, in which molecular entities with the same electronic structure and same number of valence electrons have similar chemistries,¹ the understanding of the key concepts surrounding molecular structure and chemical bonding along with the reactivity of isovalent species has improved our knowledge of the chemistries of main group XIV to XVI elements. Specifically, the chemistries of molecules containing main group XIV and XVI elements silicon (Si) and sulfur (S), which hold four and six valence electrons, respectively, have often been compared to their carbon (C) and oxygen (O) analogues,²⁻⁵ with emphasis on, e.g., the energies and stabilities of $X=Y$ ($X = C, Si$; $Y = O, S$) double bonds.⁶⁻¹¹ While the carbon-oxygen double bond has been well-established for more than a century with typical bond lengths of 1.16 to 1.21 Å and bond strengths of about 700 to 900 kJ mol⁻¹,^{12,13} molecules containing double bonds between third period elements had been originally labeled as ‘non-existent compounds’¹⁴ until the early 1970s. Since then, various species comprising multiply bonded heavy elements have been synthesized¹⁵⁻¹⁸ including members of the silanethione (R_2SiS) family. The first silanethione compound detected experimentally, the 2,4,6-triisopropylphenyl-2,4,6-tris[bis(trimethylsilyl)methyl]phenylsilanethione molecule, was isolated by Suzuki et al.,¹⁹ in which the product was stabilized by bulky substituents. More recently, the parent silanethione, H_2SiS (**5**) (Figure 1), was characterized in a gas discharge of silane (SiH_4) and hydrogen sulfide (H_2S) using rotational spectroscopy by Thorwirth et al.²⁰ and by matrix isolation infrared spectroscopy by Liu et al.; the latter work also characterized the high energy isomer: thiohydroxysilylene ($HSiSH$; **6**, **7**).⁵ Silanethione (H_2SiS ; **5**) and singlet thiohydroxysilylene ($HSiSH$; **6**, **7**) are the third period analogues of formaldehyde (H_2CO ; **1**) and singlet hydroxymethylene ($HCOH$; **2**, **3**), respectively. These isovalent species have identical point groups and molecular structures (Figure 1) with the greatest difference being their bond lengths.²¹⁻²⁴ This is primarily due to the larger atomic radius of silicon and its tendency to form weaker bonds than carbon, and the singlet-triplet gaps of the carbene-type species are reduced from 114 kJ mol⁻¹ in case of thiohydroxysilylene ($HSiSH$; **6-8**) to 87 kJ mol⁻¹ for hydroxymethylene ($HCOH$; **2-4**). Notably, silanethione (H_2SiS ; **5**) and its *cis/trans*-thiohydroxysilylene isomers ($HSiSH$; **6**, **7**) are much closer in energy than formaldehyde (H_2CO ; **1**) and hydroxymethylene ($HCOH$; **2**, **3**) of 48–58 kJ mol⁻¹ compared to 221–239 kJ mol⁻¹,^{25,26} reinforcing the idea that silicon-sulfur double bonds are weaker than their carbon-oxygen counterparts.⁷⁻⁹ Due to these differences, silanethione

(H₂SiS; **5**) makes an ideal target of a directed synthesis to uncover information on the chemical reactivity and chemical dynamics of molecules containing both silicon and sulfur.

Besides chemical bonding and electronic structure, molecules incorporating silicon and sulfur are also of interest to the astrochemistry community. There have been over 200 molecules discovered in the interstellar medium (ISM) and circumstellar envelopes (CSEs), of which 13 contain silicon and 31 contain sulfur; the only interstellar molecule containing both silicon and sulfur is silicon monosulfide (SiS).²⁷ Silicon monosulfide has been observed in the CSEs of some 20 low to intermediate mass late-type carbon- and oxygen-rich Asymptotic Giant Branch (AGB) stars with mean fractional gas phase abundances of 3.1×10^{-6} and 2.7×10^{-7} , respectively.²⁸ SiS is particularly abundant in the CSE of the carbon-rich star IRC+10216, where roughly one third of the molecules contain silicon and/or sulfur.²⁹ As the simplest silicon- and sulfur-containing closed-shell molecule after silicon monosulfide, the hydrogenated form – silanethione (H₂SiS; **5**) – is expected to be formed in interstellar environments. However, despite the high abundance of silicon monosulfide, silanethione (H₂SiS; **5**) has not been detected in deep space yet. An understanding of the driving mechanisms behind the formation of silanethione (H₂SiS; **5**) could elucidate the chemical conditions necessary for synthesis and give insight to why it has not yet been found in space.

Here, we unveil chemical dynamics of the bimolecular reaction of the D1-silyldiyne radical (SiD; X²Π) with deuterium sulfide (D₂S) and with hydrogen sulfide (H₂S) leading to D2/D1-silanethione (D₂SiS/DHSiS) along with the D1-thiosilaformyl radical (DSiS) under single-collision conditions utilizing crossed molecular beams experiments coupled with electronic structure calculations and astrochemical modeling. Hydrogen sulfide (H₂S) has been detected in star forming regions such as Orion-KL;³⁰ the silyldiyne radical (SiH; X²Π) has been tentatively detected in the same source.³¹ While the silyldiyne detection has not been confirmed,³² a synthetic pathway to silanethione in the interstellar medium via the reaction of the silyldiyne radical with hydrogen sulfide is plausible. Note that for the SiD/D₂S system, there are two reaction channels: the first leading to D2-silanethione (D₂SiS) via atomic deuterium (D) loss (reaction 1) and the second forming D1-(iso)thiosilaformyl (DSiS/DSSi) radicals via molecular deuterium (D₂) loss (reaction 2). In order to acquire additional information on the position of the atomic (H/D) and molecular (HD/H₂) hydrogen losses and the inherent reaction mechanisms, the reaction of the D1-

silyldiyne radical with hydrogen sulfide was also conducted (reactions 3–6). This system also serves to explore the chemical bonding between silicon and sulfur by initiating a single-collision event between the D1-silyldiyne radical transient and the simplest closed-shell sulfur hydride, hydrogen (deuterium) sulfide. Under these experimental conditions, successive reactions and hydrogen-assisted isomerization processes, that would cause the nascent reaction products to change such as in bulk experiments, can be excluded,³³ and the species detected here represent the primary, unchanged reaction products.



2. Experimental Methods

Reactive scattering experiments of D1-silyldiyne radicals (SiD ; $X^2\Pi$) with deuterium sulfide (D_2S ; 98.8 % D atom; Sigma-Aldrich) and hydrogen sulfide (H_2S ; ≥ 99.5 %; Sigma-Aldrich) were conducted in a crossed molecular beams machine under single collision conditions.³⁴ The $\text{SiD}/\text{D}_2\text{S}$ reaction was explored to unravel the chemical dynamics of the atomic (D) and molecular deuterium (D_2) loss pathways (reactions (1)–(2)), whereas the $\text{SiD}/\text{H}_2\text{S}$ reaction was conducted to gain additional information on the position of atomic (H/D) and/or molecular hydrogen loss (HD/H_2) (reactions (3)–(6)). The setup consists of a 2.3 m³ stainless steel box that is pumped by three 2.0 m³ s^{−1} magnetically suspended compound molecular pumps (TG2003MCA, Osaka Vacuum) backed by a 0.010 m³ s^{−1} scroll pump (XDS35, Boc Edwards) to the low 10^{−8} Torr region; pressures of a few 10^{−9} Torr are achievable by baking the main chamber. Housed in the main chamber are two source chambers and a triply differentially pumped detector that is rotatable in the scattering plane defined by both molecular beams. Each source chamber is pumped by a 2.0 m³ s^{−1} (TG2003MCA, Osaka Vacuum) and 0.40 m³ s^{−1} (TG420 MCAC, Osaka Vacuum) maglev pump backed by a 0.14 m³ s^{−1} roots blower (RUVAC WSU 501, Leybold) and 0.008 m³ s^{−1} scroll pump (GVSP30, Boc Edwards) to the mid 10^{−9} Torr region.³⁵ The detector is composed of three differentially pumped regions: I and II reduce the gas load from the main chamber (with region II

also containing the quadrupole mass spectrometer (QMS; QC 150, Extrel) and Daly-type³⁶ detector) and III contains a modified Brink-type³⁷ electron impact ionizer (80 eV) surrounded by a liquid nitrogen-cooled cold shield. Regions I, II, and III are pumped by two $0.43 \text{ m}^3 \text{ s}^{-1}$ (TG410MCA, Osaka Vacuum) and one $0.29 \text{ m}^3 \text{ s}^{-1}$ (TH261MCA, Osaka Vacuum) maglev pump, respectively; all pumps are backed by a $0.43 \text{ m}^3 \text{ s}^{-1}$ (TG403M, Osaka Vacuum) maglev and $0.005 \text{ m}^3 \text{ s}^{-1}$ scroll pump to reach pressures as low as 6×10^{-12} Torr in region III; lower pressures of 8×10^{-13} Torr are available by operating a 4 K cold head in region III. Neutral products that enter the detector are ionized and filtered by mass-to-charge (m/z) ratio in the QMS. Ions that passed through the filter were accelerated to an aluminum-coated stainless-steel target (-22.5 kV) creating a cascade of secondary electrons. These were directed to an aluminum-coated organic scintillator (BC-418, Saint Gobain) which generated a photon pulse that was collected by a photomultiplier tube (PMT; Model 8850, Burle) operating at -1.35 kV . The resulting signal passed through a discriminator set at 1.6 mV (Model F-100TD, Advanced Research Instruments) and was recorded by a multichannel scaler (MCS; Model 430, Stanford Research Systems), which files the signal in a series of $10.24 \text{ } \mu\text{s}$ time bins to obtain the time-of-flight (TOF) spectra. An optimized pulse sequence was used to coordinate the data collection (Supplementary Note 1). Note that the machine is equipped with an oxygen-free high conductivity (OFHC) copper shield located $7.4 \pm 0.6 \text{ mm}$ downstream from the chopper wheel and $8.1 \pm 0.1 \text{ mm}$ upstream from the interaction region to reduce the background pressure in the detector from straight-through molecules. The cold shield is cooled to 10 K via a cold head (Model 1020, CTI-Cryogenics) which further reduces pressure in the main chamber to the mid 10^{-9} Torr region and also prevents straight-through molecules from reaching the ionizer.

A pulsed supersonic beam of D1-silylidyne radicals was produced *in situ* by laser ablation of a silicon rod (Si; 99.999 %; Goodfellow Cambridge Limited) with the fourth harmonic output of a neodymium-doped yttrium aluminum garnet (Nd:YAG) laser (Quanta-Ray Pro 270, Spectra-Physics) operating at 30 Hz and $5\text{--}12 \text{ mJ}$ and entraining the ablated species in a 1:1 gas mixture of neon (Ne; 99.999 %; Airgas) and deuterium (D_2 ; 99.999 % purity; $\geq 99.75\%$ D atom; Linde) at a backing pressure of 3040 Torr .³⁸⁻⁴¹ As a seeding gas, molecular deuterium (D_2) led to a low intensity of the D1-silylidyne beam and a significant fraction of metastable species, whereas addition of neon (Ne) was found to quench metastable D1-silylidyne radicals thus increasing D1-silylidyne availability for the crossed beam reaction. The 266 nm output was tightly focused by a

plano-convex lens (PLCX-25.4-1030.2-UV-266, CVI) to a spot size of less than 1.5 mm^2 onto a silicon rod that was kept in helical motion by a motor (SP18074-3606).⁴² In addition to acting as a seeding gas, the neon/deuterium mixture provided the reactant (D_2), most likely undergoing atomic deuterium abstraction by atomic silicon to form D1-silyldiyne radicals.³⁸ Considering the isotopic abundances of silicon (92.2297 % ^{28}Si ; 4.6832 % ^{29}Si ; 3.0872 % ^{30}Si) and that the fraction of D1-silyldiyne to silicon in the primary beam was $8 \pm 1 \%$, the D1-silyldiyne beam was optimized at $m/z = 31$ for ^{29}SiD to avoid overlap with silicon at $m/z = 30$ (^{30}Si). If D1-silyldiyne radicals are formed in the $\text{A}^2\Delta$ excited state, their lifetime of about 500 ns causes them to decay to the ground state during the travel time of $39 \mu\text{s}$ to the interaction region.⁴³ The D1-silyldiyne beam passed first through a stainless-steel skimmer located $18.0 \pm 0.1 \text{ mm}$ downstream of the primary pulsed valve nozzle, then through the slit of a chopper wheel located $11.6 \pm 0.6 \text{ mm}$ downstream of the skimmer, which selected a peak velocity (v_p) of $1142 \pm 29 \text{ m s}^{-1}$ and speed ratio (S) of 6.2 ± 1.1 (Table 1). A precision motion controller (MC 5005 S RS, Faulhaber) was coupled to the chopper wheel motor (2057S024B, Faulhaber). The signal period stability of $2083.3 \pm 0.1 \mu\text{s}$ when operating at 480 Hz was ascertained with a digital oscilloscope (TDS 2024B, Tektronix). In the secondary source chamber, a pulsed deuterium sulfide beam ($v_p = 801 \pm 21 \text{ m s}^{-1}$; $S = 12.8 \pm 0.8$) at a backing pressure of 550 Torr passed a skimmer located $18.0 \pm 0.1 \text{ mm}$ downstream of the secondary pulsed valve nozzle before crossing perpendicularly with the D1-silyldiyne beam. This resulted in a collision energy (E_c) of $15.9 \pm 0.9 \text{ kJ mol}^{-1}$ and center-of-mass (CM) angle (Θ_{CM}) of $40.8 \pm 1.5^\circ$; experiments carried out with hydrogen sulfide ($v_p = 805 \pm 9 \text{ m s}^{-1}$; $S = 12.4 \pm 0.1$) gave an E_c of $15.6 \pm 0.6 \text{ kJ mol}^{-1}$ and Θ_{CM} of $39.4 \pm 1.0^\circ$.

Up to 2×10^6 TOF spectra were recorded at angles between $15 \leq \Theta \leq 65^\circ$ with respect to the D1-silyldiyne beam ($\Theta = 0^\circ$), then integrated and normalized with respect to the CM angle intensity to give the laboratory angular distribution. To understand the dynamics of the reaction, the time- and angular-dependent laboratory data must be converted to the CM reference frame. This was done with a forward convolution routine accounting for apparatus performances, velocity spreads, and beam divergences to create user-defined CM translational energy ($P(E_{\text{T}})$) and angular ($T(\theta)$) flux distributions, which were refined iteratively until an admissible fit of the laboratory data was attained.^{44,45} The CM functions describe a product flux contour map which reveals the differential reactive cross section $I(u, \theta) \sim P(u) \times T(\theta)$ as intensity with respect to the angle θ and the CM velocity u .⁴⁶ The energy dependence of the reactive scattering cross-section of a

barrierless, exoergic reaction is accounted for by utilizing the intermolecular, attractive dipole-dipole interaction potential between reactant species giving a reactive scattering cross-section of $E_T^{-2/3}$ energy dependence.⁴⁷

3. Computational

The theoretical calculations were performed using the GAMESS-US⁴⁸ and MOLPRO⁴⁹ packages. Restricted wavefunctions were utilized in order to avoid spin contamination; no symmetry restrictions were imposed in the geometry optimizations. For a preliminary exploration of the potential energy surface (PES), density functional theory (DFT)⁵⁰ calculations were employed with the M06-2X⁵¹ exchange and correlation functional along with the cc-pV(T+d)Z basis set.⁵²⁻⁵⁴ At all obtained minima and transition states, the Hessian matrix was calculated to perform a vibrational analysis of all possible isotopologues here studied, from where all zero-point energy (ZPE) corrections were obtained at the M06-2X/cc-pV(T+d)Z level. Intrinsic reaction coordinate (IRC) calculations starting from all transition states (TS) were executed to ensure the correct connection paths. After the initial exploratory part, all structures were reoptimized using the more accurate coupled-cluster singles and doubles plus perturbative triples^{55,56} (CCSD(T)) with the aug-cc-pV(T+d)Z basis set. At this level, the Hessian matrix was calculated and a vibrational analysis for the non-deuterated case only was performed, to make sure that the structures were still minima or transition states on the coupled-cluster PES. To further improve the energetic results, a single point energy using the explicitly correlated CCSD(T)-F12^{57,58} method was employed. This highly accurate PES, termed as CCSD(T)-F12/aug-cc-pV(T+d)Z//CCSD(T)/aug-cc-pV(T+d)Z+ZPE(CCSD(T)/aug-cc-pV(T+d)Z), can be seen in the schematic representation given in Figure S2 and it generally shows an accuracy within 4 kJ mol⁻¹.⁵⁹

Finally, to obtain the ZPE corrected energies for the isotopic substitutions considered in this work, calculations of the vibrational frequencies using the M06-2X/cc-pV(T+d)Z level for all possible deuteration scenarios (the fully deuterated case, the case with one deuterium at each possible position, and the non-deuterated case) were conducted. These energies are therefore represented as CCSD(T)-F12/aug-cc-pV(T+d)Z//CCSD(T)/aug-cc-pV(T+d)Z+ZPE(M06-2X/cc-pV(T+d)Z). Note that for the non-deuterated case (SiH+H₂S), in which we have both the CCSD(T) and M06-2X values for the ZPE, a comparison shows that the maximum deviation between

CCSD(T) and DFT computed ZPEs is of only 0.6 kJ mol⁻¹. For this reason, it was deemed unnecessary to calculate the ZPE of all isotopic variants using the highly expensive CCSD(T) method. All structures and parameters are listed in Table S1.

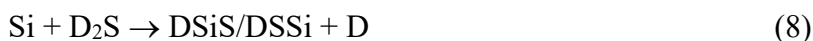
4. Astrochemical Modeling

Since the well-defined conditions in a laboratory setting cannot fully replicate the complexity of the interstellar medium (ISM), astrochemical modeling is used to evaluate the effect of the reaction of silyldiyne (SiH) with hydrogen sulfide (H₂S) on the observability of the atomic and molecular hydrogen loss products silanethione (H₂SiS) and the (iso)thiosilaformyl (HSiS/HSSi) radical. Silicon is heavily depleted from the gas phase in the interstellar medium with 90–99 % of its cosmic abundance incorporated into refractory dust grains. In cold clouds, the remaining gas-phase silicon is accreted onto the icy mantles of the grains and likely converted to silane (SiH₄) consistent with the non-detection of silicon monoxide (SiO) to levels of a few times 10⁻¹² relative to molecular hydrogen.^{60,61} Silicon monoxide has been detected, however, in hot molecular cores⁶² where ice mantles have been returned to the gas through heating and in shocked regions,⁶³ in some of which very high abundances indicate that the shock velocity is high enough to destroy grains cores. In these environments, reactive silicon species can be increased by up to six orders of magnitude in comparison to cold molecular clouds.^{61,64} Here, the newly explored reaction of silyldiyne radicals with hydrogen sulfide was incorporated in chemical models of three regions in the Orion Kleinmann-Low Nebula, i.e. the Orion 15.5 km s⁻¹ component (O15), the Orion Hot Core (OHC), and the Orion Plateau (OPI).⁶⁵ The physical conditions of these sources are presented in Table S2. Due to the 100 to 225 K temperature range of these sources, the model focuses on silane (SiH₄) and hydrogen sulfide (H₂S) that have been thermally desorbed along with grain ice mantles with initial fractional abundances of 2×10^{-7} and 2×10^{-6} , respectively, the latter value consistent with the abundance of hydrogen sulfide detected in the Orion Hot Core by Crockett et al (2014).⁶⁶ The silyldiyne radical can be formed from silane by a series of reactions involving cosmic ray-induced degradation and also by proton-transfer followed by dissociative recombination with electrons. The calculations of the fractional abundances begin at $t = 0$, when the ice mantles are injected into the gas phase, then follow the subsequent time-dependent chemistry up to 5×10^5 years using the DVODE package to solve the system of kinetics equations.⁶⁷ We have added over 40 gas-phase reactions to describe the chemistries of H₂SiS and

HSiS using the trajectory scaling approximation⁶⁸ to calculate ion-neutral rate coefficients for the destruction of H₂SiS and HSiS/HSSi since their electric dipole moments are large, i.e. 2.67 D²⁰ and 2.044 D,²³ respectively. The newly formed molecules also react with radicals such as hydroxyl (OH) via neutral-neutral reactions. Our final reaction set is an extension of the UMIST Database for Astrochemistry⁶⁹ and consists of 6229 reactions among 472 species. In our calculations we derive a total rate coefficient of $6 \times 10^{-10} \text{ cm}^3 \text{ s}^{-1}$ for the silyldiyne – hydrogen sulfide reaction and equal branching to H₂SiS and HSiS.

5. Results & Discussion

5.1. Laboratory System. Due to the presence of atomic silicon (Si(³P)) *and* D1-silyldiyne (SiD; X²Π) in the supersonic primary beam, both atomic silicon (Si(³P)) *and* D1-silyldiyne (SiD; X²Π) react with deuterium sulfide (D₂S) and with hydrogen sulfide (H₂S). However, the chemical dynamics of the Si(³P)–D₂S and Si(³P)–H₂S systems were untangled earlier;^{65,70} these experiments revealed reactive scattering signal at mass-to-charge ratios of 60 and 62 as well as 60 and 61, respectively, thus revealing the molecular hydrogen (deuterium) loss channel (reactions (7) and (9)) and the atomic hydrogen/deuterium elimination pathway (reactions (8) and (10)). Feasible mass combinations for these systems are compiled in Tables S3 and S4. It is important to highlight that for the SiD–D₂S/H₂S systems, due to the additional deuterium atom from the D1-silyldiyne reactant, the reaction channels of the SiD–D₂S/H₂S systems can be discriminated from the Si–D₂S/H₂S reaction due to differences in mass-to-charge ratios (Tables S5 and S6). The corresponding Newton diagrams and recoil circles of the heavy reaction products are presented in Figures 2 and 3. This methodology has been applied earlier in our laboratory to extract the distinct chemical dynamics of the Si–SiH₄⁷¹ and SiD–SiH₄⁷² systems.



5.1.1. SiD–D₂S System. Reactive scattering signal for the reaction of the D1-silyldiyne radical (SiD; X²Π) with deuterium sulfide (D₂S) was searched for at $m/z = 62$ and 64 to probe the molecular and atomic deuterium loss channels yielding – after ionization – signal for D²⁸Si³²S⁺ ($m/z = 62$) and D₂²⁸Si³²S⁺ ($m/z = 64$) (Figure 4). Signal at $m/z = 62$ was observed; this signal could

originate in principle from three sources: i) $D^{28}Si^{32}S^+$ fragment ions from the dissociative electron impact ionization of the $D_2^{28}Si^{32}S$ isomer(s) of the atomic deuterium loss channel (reaction (1)), ii) ionized reaction products of the molecular deuterium loss channel ($D^{28}Si^{32}S^+$) (reaction (2)), and iii) ionized reaction products from the atomic deuterium loss channel of the Si– D_2S system ($D^{28}Si^{32}S^+$) (reaction (8)). Unfortunately, at $m/z = 64$ there was high background counts originating from dissociative electron impact ionization of deuterium disulfide (D_2S_2) – a minor impurity in the gas cylinder – yielding $^{32}S_2^+$; this background concealed any reactive scattering signal at $m/z = 64$. The TOF spectra (Figure 4) at $m/z = 62$ show two distinct peaks with maxima at about 300–350 (fast component) and 500 μs (slow component) suggesting that more than one reaction channel is involved. These TOF spectra were normalized with respect to the CM angle and integrated to obtain the laboratory angular distribution (LAD), which spans from 19.25° to 59.25° ; this distribution is nearly symmetric around the CM angle. Additional information can be obtained by examining the Newton diagrams for the atomic and molecular deuterium loss channels for the SiD– D_2S system as well as for the atomic deuterium loss pathway of the Si– D_2S reaction (Figure 2). The vectors along the x- and y-axes of the diagram correspond to the most probable velocities of the deuterium sulfide and silicon/D1-silylidyne reactant beams. Note that the atomic silicon is carried within the D1-silylidyne beam causing them to have the same velocity, but slightly different center-of-mass angles. The radii of the recoil circles represent the maximum CM velocity of the reactively scattered heavy products; each circle spans an angular range in which the corresponding product is expected to be observed by the detector. At $m/z = 62$, the LAD clearly depicts ion signal at angles outside the predicted range for the atomic deuterium loss channel and DSiS/DSSi heavy product of the Si– D_2S Newton circle (magenta); this finding reveals that the D and/or D_2 loss channels in the SiD– D_2S system are open.

5.1.2. SiD– H_2S System. Signal for the reaction of the D1-silylidyne radical (SiD; $X^2\Pi$) with hydrogen sulfide (H_2S) was scanned at $m/z = 60$ to 63 to probe for the atomic hydrogen loss ($HD^{28}Si^{32}S^+$, $m/z = 63$) (reaction (3)), the atomic deuterium loss ($H_2^{28}Si^{32}S^+$, $m/z = 62$; $H_2^{29}Si^{32}S^+/H_2^{28}Si^{33}S^+$, $m/z = 63$) (reaction (4)), molecular hydrogen loss ($D^{28}Si^{32}S^+$, $m/z = 62$; $D^{29}Si^{32}S^+/D^{28}Si^{33}S^+$, $m/z = 63$) (reaction (5)), and hydrogen deuteride loss ($H^{28}Si^{32}S^+$, $m/z = 61$; $H^{29}Si^{32}S^+/H^{28}Si^{33}S^+$, $m/z = 62$; $H^{30}Si^{32}S^+/H^{29}Si^{33}S^+/H^{28}Si^{34}S^+$, $m/z = 63$) (reaction (6)). These studies revealed the following findings. *First*, signal was observed at $m/z = 63$. Since no signal at $m/z = 63$ was observed in the Si– H_2S system, signal at $m/z = 63$ is *unique* to the SiD– H_2S reaction

revealing the atomic hydrogen loss channel and formation of $\text{HD}^{28}\text{Si}^{32}\text{S}$ isomer(s). The TOF spectra at $m/z = 63$ (Figure 5) show a single peak at about 500 μs with the nearly symmetric LAD spanning from 17.25° to 57.25° . This pattern is similar to the slow component of the SiD–D₂S system recorded at $m/z = 62$ suggesting that the dominating contributor to $m/z = 62$ in the SiD–D₂S system might indeed be dissociative electron impact ionization of the neutral D₂SiS product formed via the atomic deuterium loss.

Second, signal was also observed at $m/z = 62$. The corresponding TOFs (Figure 6) distinctly show two peaks at 300–350 μs and 500 μs with the LAD ranging from 17.25° to 42.25° . This pattern mirrors the finding of the SiD–D₂S system discussed above: a fast component of the molecular and a slow component of the atomic deuterium loss channels with the latter originating from dissociative electron impact ionization of the neutral D₂SiS product. Therefore, in the SiD–H₂S system, signal at $m/z = 62$ supports the existence of the atomic hydrogen loss channel (HDSiS isomers) and of the molecular hydrogen loss pathway (DSiS isomers). Note that significant background counts at $m/z = 62$ closer to the secondary beam limited the experimentally recorded angular range. The aforementioned findings are also supported by the Newton diagram of the SiD–H₂S system depicting the H, D, and H₂ loss channels (Figure 3). The angular range of the hydrogen atom loss recoil circle matches the LAD for $m/z = 63$ providing additional evidence for the formation of the $\text{HD}^{28}\text{Si}^{32}\text{S}$ isomer(s), i.e. at least the $\text{HD}^{28}\text{Si}^{32}\text{S}$ species. The LAD for $m/z = 62$ has a similar shape as $m/z = 63$ prior to a noticeable broadening at lower angles; this suggests additional contributions from the molecular hydrogen loss channel forming DSiS isomer(s) due to its wider recoil circle. This finding also correlates with the TOF spectra, i.e. the presence of two distinct peaks. For $m/z = 62$, this is once again indicative that products are formed from the molecular hydrogen loss pathway (fast signal) and the H and/or D loss pathways (slow signal). Finally, it is important to note that signal was also observed at $m/z = 60$ and 61 at the CM angle; however, the data were ill constrained due to the uncertainty in multichannel fits.

5.2. Center-of-Mass System. To elucidate the chemical dynamics of the SiD–D₂S/H₂S systems, the laboratory data were transformed from the laboratory into the CM reference frame to obtain the $P(E_{\text{T}})$ and $T(\theta)$.

5.2.1. SiD–D₂S System. *First*, for the SiD–D₂S system, the slow, more intense contribution of the TOF spectra (Figure 4) at $m/z = 62$ could be replicated through a single-channel fit for the reaction

SiD (30 amu) + D₂S (36 amu) → D₂SiS (64 amu) + D (2 amu) with $m/z = 62$ originating from dissociative electron impact ionization of the nascent product ions at $m/z = 64$ (Figure 7). **Second**, the fast peak was fit via a single channel of the reaction SiD (30 amu) + D₂S (36 amu) → DSiS (62 amu) + D₂ (4 amu). These two channels were able to replicate the experimental data at $m/z = 62$ with overall branching ratios^{73,74} of $43 \pm 8 \%$ and $57 \pm 8 \%$ for the atomic and molecular deuterium loss channels, respectively (Figure 4 (*top*)). However, recall that $m/z = 62$ could also be a contributor from the Si–D₂S reaction,⁶⁵ i.e. the formation of D²⁸Si³²S isomers. To objectively account for this possibility, we also attempted to fit the LAD distribution at $m/z = 62$ with three components (Figure 4 (*bottom*)) extracting the CM functions of the deuterium loss channel ($m/z = 62$) for the Si–D₂S system from Doddipatla et al.⁶⁵ Here, we could add contributions from the Si–D₂S reaction of up to $2 \pm 1 \%$ and overall fractions for the SiD–D₂S system of $44 \pm 7 \%$ and $54 \pm 10 \%$ for the atomic and molecular deuterium loss channels, respectively.

For the slow channel (atomic deuterium loss) forming D₂SiS isomer(s), the $P(E_T)$ (Figure 7A) exhibits a maximum translational energy, E_{\max} , of $64 \pm 17 \text{ kJ mol}^{-1}$ for those products without internal excitation. Conservation of energy dictates that $E_{\max} = E_C - \Delta_r G$ where E_C is the collision energy of the reaction ($15.9 \pm 0.9 \text{ kJ mol}^{-1}$) and $\Delta_r G$ the reaction energy. This reveals that the reaction to form D₂SiS plus atomic deuterium is exoergic by $-48 \pm 18 \text{ kJ mol}^{-1}$. The $P(E_T)$ depicts a peak at 14 kJ mol^{-1} suggesting that there is a tight exit transition state from the decomposing D₃SiS intermediate(s) to the D₂SiS plus D products. The best fit $T(\theta)$ (Figure 7B) shows that the products have equal scattering probability in all directions; further, a forward-backward symmetry is clearly observable. These findings suggest indirect scattering dynamics through D₃SiS intermediate(s), with lifetimes longer than the rotational period(s). Second, the $P(E_T)$ for the fast channel (molecular deuterium loss) leading to DSiS/DSSi isomer(s) (Figure 8A) shows an E_{\max} of $162 \pm 21 \text{ kJ mol}^{-1}$, revealing that the reaction to form DSiS/DSSi plus D₂ is exoergic by $-146 \pm 22 \text{ kJ mol}^{-1}$. The $P(E_T)$ depicts a peak at 119 kJ mol^{-1} indicating a tight exit transition state and significant electron redistribution from the decomposing D₃SiS intermediate(s) to the DSiS/SiSD plus D₂ products. The $T(\theta)$ (Figure 8B) shows forward-backward symmetry and that the products have equal scattering probability in all directions, which suggests indirect scattering dynamics through long-lived D₃SiS intermediate(s). To summarize, the SiD–D₂S system revealed the existence of at least two channels: i) D₂SiS (64 amu) + D (2 amu) and ii) DSiS (62 amu) + D₂ (4 amu) with branching ratios of $43 \pm 8 \%$ and $57 \pm 8 \%$, respectively.

5.2.2. SiD/H₂S System. For the SiD–H₂S system, the TOFs at $m/z = 63$ (Figure 5) were fit with a single channel corresponding to the reaction SiD (30 amu) + H₂S (34 amu) → HDSiS (63 amu) + H (1 amu) (Figure 9). The CM functions used were nearly identical to those for the deuterium loss channel fit of the slow peak for the SiD–D₂S system. The $P(E_T)$ (Figure 9A) shows an E_{\max} of $63 \pm 13 \text{ kJ mol}^{-1}$ revealing a reaction energy of $-47 \pm 14 \text{ kJ mol}^{-1}$; the distribution further reveals a maximum of 18 kJ mol^{-1} suggesting an exit barrier from H₂DSiS intermediate(s) to form the HDSiS/HSiSD/DSiSH products. The $T(\theta)$ (Figure 9B) is nearly isotropic and forward-backward symmetric implying an indirect reaction with a long-lived intermediate.

The TOFs at $m/z = 62$ had a fast and slow component (Figure 6). The slow peak could be fit with identical CM functions as those used for the TOFs at $m/z = 63$ (Figure 9) indicating that the slow component of the TOFs at $m/z = 62$ originates from dissociative electron impact ionization of the $m/z = 63$ products (HDSiS) formed via SiD (30 amu) + H₂S (34 amu) → HDSiS (63 amu) + H (1 amu). It is important to note that in principle, the slow component of $m/z = 62$ could also originate from the formation of H₂SiS plus atomic deuterium: SiD (30 amu) + H₂S (34 amu) → H₂SiS (62 amu) + D (2 amu); this fit is shown in Figure 6 (*middle*). Finally, a third fit utilizing *both* the dissociative electron impact ionization channel of $m/z = 63$ and the atomic deuterium pathway leading to H₂SiS (62 amu) could reproduce the experimental data with branching ratios of $75 \pm 4 \%$ and $25 \pm 4 \%$, respectively (Figure 6 (*bottom*)). Overall, the slow peak at $m/z = 62$ can originate from the HDSiS (63 amu) + H (1 amu) (dissociative electron impact ionization) *and/or* H₂SiS (62 amu) + D (2 amu). Hereafter, the fast component was fit with a single channel corresponding to the SiD (30 amu) + H₂S (34 amu) → DSiS (62 amu) + H₂ (2 amu) channel. Figure 10A shows the $P(E_T)$ for the H₂ loss channel, which results in an E_{\max} of $162 \pm 21 \text{ kJ mol}^{-1}$ and reaction energy of $-146 \pm 22 \text{ kJ mol}^{-1}$; this data is within the error range identical to that of the D₂ loss channel from the SiD–D₂S reaction: SiD (30 amu) + D₂S (36 amu) → DSiS (62 amu) + D₂ (4 amu). Further, the $P(E_T)$ shows a maximum at 124 kJ mol^{-1} indicating once again a tight exit transition state from H₂DSiS intermediates to the DSiS/SiSD products. The $T(\theta)$ (Figure 10B) is also isotropic and forward-backward symmetric suggesting long-lived intermediate(s) and indirect scattering dynamics. To summarize, the SiD–H₂S system provided evidence on the existence of at least two channels: i) DSiS (62 amu) + H₂ (2 amu) and ii) HDSiS (63 amu) + H (1 amu) and

possibly H_2SiS (62 amu) + D (2 amu) with branching ratios of $72 \pm 9 \%$, $21 \pm 5 \%$, and $7 \pm 3 \%$, respectively.

5.3. Potential Energy Surface. The experimental results and electronic structure calculations can be merged to obtain further information on the dynamics of the reactions. The calculated PES for the $\text{SiD-D}_2\text{S}$ system is shown in Figure 11. The D1-silyldyne radical undergoes barrierless addition to one of the lone electron pairs of sulfur of the deuterium sulfide to form intermediate **i1a** and/or **i1b**; these two intermediates may isomerize to one another via a bond rotation through a transition state at -54 kJ mol^{-1} relative to the separated reactants. Intermediate **i1a** can form product **p2** via molecular deuterium (D_2) loss through a tight transition state or isomerizes by atomic deuterium migration to **i2** through a tight transition state located 31 kJ mol^{-1} above **i1a**; intermediate **i1b** also isomerizes to **i2** through a barrier 28 kJ mol^{-1} above **i1b**. At this point, **i2** can isomerize by deuterium migration to **i3** or forms products **p2** (D_2 loss; tight exit transition state), **p3** (D loss; exit barrier), **p4** (D loss; no exit barrier) or **p5** (D loss; no exit barrier). From **i3**, **p1** and/or **p3** are accessible; the pathway from **i3** to **p3** is barrierless as shown in Figure S5. The experimentally derived reaction energy from the D and D_2 loss channels $-48 \pm 18 \text{ kJ mol}^{-1}$ and $-146 \pm 22 \text{ kJ mol}^{-1}$ matches that of **p3** (D_2SiS ; $-39 \pm 4 \text{ kJ mol}^{-1}$) and at least **p1** (DSiS ; $-131 \pm 4 \text{ kJ mol}^{-1}$), respectively, whereas their isomers lie outside their respective error ranges. However, **p2**, **p4**, and **p5** are still possible contributors, as the E_{max} for each can cloak their contribution in the low energy portion of the $P(E_{\text{T}})$. To summarize, at least **p1** and **p3** are suggested to be formed via atomic and molecular deuterium loss, respectively, leading to D2-silanethione (D_2SiS) along with the D1-thiosilaformyl radical (DSiS).

The PES for the $\text{SiD-H}_2\text{S}$ system is shown in Figure 12; this surface exhibits the same reaction pathways as the fully deuterated case plus additional routes due to the partial deuteration of the system. In this case there are three additional intermediates (**i1b'**, **i1a'**, and **i2'**), which are related to **i1b**, **i1a**, and **i2** due to the deuterium atom location, as well as additional products (**p1'**, **p2'**, **p3'**, **p4'**, **p4''**, **p5'**, **p5''**) since H, D, H_2 , or HD losses could be open. Here, **p1** and **p1'** are formed via the similar pathway as in the fully deuterated case, with **p1** formed through molecular hydrogen (H_2) loss and **p1'** formed through hydrogen deuteride (HD) loss. The reaction energy found from the $P(E_{\text{T}})$ for the H_2 loss channel is $-146 \pm 22 \text{ kJ mol}^{-1}$, matching the computed energy of **p1** ($-135 \pm 4 \text{ kJ mol}^{-1}$); at least for the maximum energy release and reaction energy, **p2** falls outside

the error limits. For the D loss channels, these are identical as in the fully deuterated case, with one additional pathway: intermediate **i3** can isomerize by D migration to form **i2'** which can undergo D loss to form **p3'**. Intermediate **i2'** can also be accessed by D migration from **i2** to **i1b'** followed by H migration to **i2'** or rotation isomerization to **i1a'** and H migration to **i2'**. The reaction energy for the D loss channel in the SiD–H₂S system was not obtained experimentally due to the inability to discriminate between the D loss channel and the H loss channel at $m/z = 62$ (section 5.2.2.). However, for the H loss channel at $m/z = 63$, the reaction energy of $-47 \pm 14 \text{ kJ mol}^{-1}$ matches well with product **p3** ($-47 \pm 4 \text{ kJ mol}^{-1}$).

5.4. Astrochemical Modeling. The calculated abundances of silanethione (H₂SiS) and the thiosilaformyl radical (HSiS) as well as silicon monosulfide (SiS) and hydrogen sulfide (H₂S) following ice mantle sublimation at $t = 0$ are shown in Figure 13 for the O15, OHC, and OPI regions of the Orion Kleinmann-Low nebula. The dark grey boxes represent the observed fractional abundances of silicon monosulfide (SiS) (Table S7), whose dominant formation pathway via the reaction of atomic silicon with hydrogen sulfide was recently studied by Doddipatla et al.⁶⁵ These values are defined as the measured column density of silicon monosulfide (SiS) ($N(\text{SiS})$) divided by that of molecular hydrogen (H₂) ($N(\text{H}_2)$), with errors determined by Tercero et al.⁷⁵ However, $N(\text{H}_2)$ is difficult to measure accurately, so the light grey area in Figure 13 reveals the fractional abundance of silicon monosulfide (SiS) with an increase by a factor of three in the error of $N(\text{H}_2)$. For times between 10^4 and 2×10^5 years, thought to be typical of the ages of hot molecular cores, the calculated fractional abundance of silicon monosulfide (SiS) is in agreement with the observed values in the OHC and OPI sources. Conversely, the value does not match well in O15, which could imply that the amount of silane and/or hydrogen sulfide released from the ice mantle is a factor of 2–3 times higher than in the other two sources. For the SiH–H₂S system, similar fractional abundances of a few times 10^{-10} for the astronomically still elusive silanethione (H₂SiS) and the thiosilaformyl radical (HSiS) are predicted in OHC and O15, with those in the OPI, the coolest and least dense source, a factor of 2–4 lower. These fractional abundances translate to column densities of $(2\text{--}6) \times 10^{13} \text{ cm}^{-2}$ in OHC and O15 making the detection of both H₂SiS and HSiS feasible since rotational frequencies of H₂SiS²⁹ and HSiS⁷⁶ have been measured. Many rotational transitions of these species have already been covered, and should be searched for, in spectral line surveys of the Orion sources.^{75,77,78}

6. Conclusions

First, for the SiD–D₂S system, the crossed molecular beam experiments revealed the existence of the molecular and atomic deuterium loss channels leading to the formation of DSiS and D₂SiS isomer(s). A comparison of the experimentally derived reaction energies with the electronic structure calculations suggest that at least the D1-thiosilaformyl radical (DSiS) (**p1**) and D2-silanethione (D₂SiS) (**p3**) are formed. The reaction mechanism involves indirect scattering dynamics via the decomposition of long-lived D₃SiS intermediate(s) involving tight exit transition states both for the atomic and molecular deuterium loss channels; corresponding branching ratios of $43 \pm 8 \%$ and $57 \pm 8 \%$ were extracted experimentally. **Second**, for the SiD–H₂S system, the crossed molecular beam experiments exposed the existence of the atomic and molecular hydrogen loss channels leading to the formation of DSiS and HDSiS isomer(s) with possible contributions from an atomic deuterium pathway to H₂SiS. Branching ratios were derived to be $72 \pm 9 \%$ and $21 \pm 5 \%$ with up to $7 \pm 3 \%$ for the atomic deuterium loss. The experimentally extracted energetics of the atomic and molecular hydrogen loss channels support the preparation of at least D1-silanethione (HDSiS) (**p3**) and the D1-thiosilaformyl radical (DSiS) (**p1**) with possible contributions from silanethione (H₂SiS) (**p3'**). As for the SiD–D₂S system, the center-of-mass functions support indirect scattering dynamics via the decomposition of long-lived DH₂SiS intermediate(s) involving tight exit transition states. Which are feasible reaction pathways leading to **p1** and **p3/p3'**?

For the SiD–D₂S system (Figure 11), the D1-thiosilaformyl radical (DSiS) (**p1**) can only be formed via unimolecular decomposition of intermediate **i3**, via molecular deuterium loss through a tight exit transition state located 86 kJ mol^{-1} above the separated products. Intermediate **i3** – the silicon and sulfur isovalent species of the D3-methoxy radical (CD₃O) – can be only accessed via deuterium shift from intermediate **i2**; this species represents the isovalent counterpart of the D3-hydroxymethyl radical (CD₂OD). Intermediate **i2** in turn is accessible through a deuterium shift in **ilb** or **ila**, which can isomerize to one another by bond rotation. Note that the computations could not locate any insertion pathways to form **i2** through insertion of the silicon atom of the SiD radical into the S-D bond of deuterium sulfide; instead, all approach geometries lead to addition of the SiD radical to the sulfur atom of deuterium sulfide yielding **ila** or **ilb**. Consequently, the reaction mechanisms leading to the D1-thiosilaformyl radical (DSiS) (**p1**) are initiated by a barrierless

addition of the D1-silyldiyne radical to one of the non-bonding electron pairs of deuterium sulfide leading to intermediate **i1a** or **i1b**, which may undergo isomerization via a Si-S bond rotation to **i1b** or **i1a**, respectively. Two successive deuterium migrations lead from **i1a/i1b** to **i3**, which then undergoes molecular deuterium loss through a tight exit transition state to the D1-thiosilaformyl radical (DSiS) (**p1**). Note that in principle, intermediate **i3** could also eject a deuterium atom from the silyl group forming D2-silanethione (D₂SiS) (**p3**). The overall energy of the products of 39 kJ mol⁻¹ below the separated reactants is slightly higher than the transition state connecting **i3** and **p1** (-45 kJ mol⁻¹) and hence is competitive. However, the experiments and center-of-mass translational energy distribution proposes a tight exit transition state to form **p3** + D, which is clearly not computed for the unimolecular decomposition of **i3** to **p3** + D. However, the decomposition of intermediate **i2** to **p3** + D involves a somewhat tighter transition state, which correlates qualitatively with the experimental findings. Therefore, we may propose that D2-silanethione (D₂SiS) (**p3**) should form at least through decomposition of intermediate **i2** with possible minor contributions from intermediate **i3**. These aforementioned findings gain full support from the results of the SiD-H₂S system (Figure 12). Here, the reaction of the D1-silyldiyne radical with hydrogen sulfide commences with the barrierless addition of the silicon atom to one of the non-bonding electron pairs of hydrogen sulfide forming intermediate **i1a** or **i1b**; which may isomerize to one another via rotation around the Si-S bond. A hydrogen shift results in **i2**, which may lose atomic hydrogen through a tight exit transition state to D1-silanethione (HDSiS) (**p3**). A second hydrogen migration could convert intermediate **i2** to intermediate **i3**, which can emit molecular hydrogen via a tight exit transition state forming the D1-thiosilaformyl radical (DSiS).

Overall, our crossed molecular beams experiments of the SiD-D₂S and SiD-H₂S systems merged with electronic structure calculations provided compelling evidence on the formation of the molecular and atomic deuterium loss pathways (SiD-D₂S) and the molecular and atomic hydrogen loss pathways (SiD-H₂S) leading to the D1-thiosilaformyl radical (DSiS) (**p1**) and D2-silanethione (D₂SiS) (**p3**) as well as the D1-thiosilaformyl radical (DSiS) (**p1**) and D1-silanethione (HDSiS) (**p3**) via indirect scattering dynamics in barrierless and overall exoergic reactions. The reaction dynamics involve multiple deuterium/hydrogen shifts and tight exit transition states leading to the hitherto astronomically elusive (partially) deuterated versions of the thiosilaformyl radical (HSiS) (**p1**) and silanethione (H₂SiS) (**p3**). Astrochemical modeling suggests further that both silicon-sulfur species should be formed and observable in star forming regions under the

premise of a sufficient concentration of silylidyne radicals and readily available hydrogen sulfide. The carbon-oxygen isovalent formyl radical (HCO) and formaldehyde molecule (H₂CO, **1**) have been detected in the Orion Kleinmann-Low nebula,⁷⁹ the latter more specifically in the OHC and OPI regions.⁸⁰ While HCO and H₂CO have large differences in bond lengths and angles²³ in comparison with their isovalent counterparts HSiS (**p1**) and H₂SiS (**p3**) (Figure 1), they hold the same point groups and molecular structures. The known dipole moments of these species and rotational transitions in the laboratory suggests that the thiosilaformyl radical (HSiS) (**p1**) and silanethione (H₂SiS) (**p3**) could be detectable in the Orion Kleinmann-Low nebula. In summary, our study provides a look into the complex dynamics of silicon and sulfur chemistry and helps impart insight into silicon- and sulfur-containing molecule formation pathways in deep space.

Conflicts of Interest

There are no conflicts to declare

Acknowledgements

This work at the University of Hawaii was supported by the US National Science Foundation (CHE-1853541). TJM thanks the UK Science and Technology Facilities Council for support through grant number ST/P000312/1. BRLG also acknowledges the support from the Brazilian funding agencies CAPES, CNPq and FAPEMIG.

References

1. I. Langmuir, *Journal of the American Chemical Society*, 1919, **41**, 868-934.
2. P. J. Bruna and F. Grein, *Chemical Physics*, 1992, **165**, 265-279.
3. A. F. Jalbout and A. M. El-Nahas, *Journal of Molecular Structure: THEOCHEM*, 2004, **671**, 125-132.
4. D. Chesnut, *Chemical Physics*, 2006, **327**, 327-334.
5. X. Liu, X. Liu and X. Wang, *The Journal of Physical Chemistry A*, 2018, **122**, 7023-7032.
6. T. Kudo and S. Nagase, *Organometallics*, 1986, **5**, 1207-1215.
7. M. W. Schmidt, P. N. Truong and M. S. Gordon, *Journal of the American Chemical Society*, 1987, **109**, 5217-5227.
8. P. v. R. Schleyer and D. Kost, *Journal of the American Chemical Society*, 1988, **110**, 2105-2109.
9. J. M. Galbraith, E. Blank, S. Shaik and P. C. Hiberty, *Chemistry—A European Journal*, 2000, **6**, 2425-2434.
10. V. G. Avakyan, V. F. Sidorkin, E. F. Belogolova, S. L. Guselnikov and L. E. Gusel'nikov, *Organometallics*, 2006, **25**, 6007-6013.
11. J. X. Chen, D. Liu, C. Zhang, J. Li, H. Zhang and C. K. Kim, *Bulletin of the Korean Chemical Society*, 2015, **36**, 123-129.
12. N. N. Greenwood and A. Earnshaw, *Chemistry of the Elements*, Elsevier, 2012.
13. R. Kalescky, E. Kraka and D. Cremer, *International Journal of Quantum Chemistry*, 2014, **114**, 1060-1072.
14. W. E. Dasent, *Journal of Chemical Education*, 1963, **40**, 130.
15. P. Davidson and M. Lappert, *Journal of the Chemical Society, Chemical Communications*, 1973, 317-317.
16. N. Wiberg, *Journal of Organometallic Chemistry*, 1984, **273**, 141-177.
17. G. Raabe and J. Michl, *Chemical Reviews*, 1985, **85**, 419-509.
18. L. Pu, B. Twamley and P. P. Power, *Journal of the American Chemical Society*, 2000, **122**, 3524-3525.
19. H. Suzuki, N. Tokitoh, S. Nagase and R. Okazaki, *Journal of the American Chemical Society*, 1994, **116**, 11578-11579.
20. S. Thorwirth, J. Gauss, M. C. McCarthy, F. Shindo and P. Thaddeus, *Chemical Communications*, 2008, 5292-5294.
21. L. Nyulászi, A. Belghazi, S. K. Szétsi, T. Veszprémi and J. Heinicke, *Journal of Molecular Structure: THEOCHEM*, 1994, **313**, 73-81.
22. D.-Y. Hwang, A. M. Mebel and B.-C. Wang, *Chemical Physics*, 1999, **244**, 143-149.
23. D. E. Woon and E. Herbst, *The Astrophysical Journal Supplement Series*, 2009, **185**, 273.
24. L. Koziol, Y. Wang, B. J. Braams, J. M. Bowman and A. I. Krylov, *The Journal of Chemical Physics*, 2008, **128**, 204310.
25. Y. A. Ustynyuk, M. Nechayev, D. Laikov, N. Zemlyanskii, I. Borisova and E. Chernyshev, *Russian Chemical Bulletin*, 2001, **50**, 771-779.
26. J. M. Simmie and J. Würmel, *Journal of Physical and Chemical Reference Data*, 2020, **49**, 023102.
27. B. A. McGuire, *The Astrophysical Journal Supplement Series*, 2018, **239**, 17.
28. F. L. Schöier, J. Bast, H. Olofsson and M. Lindqvist, *Astronomy & Astrophysics*, 2007, **473**, 871-882.
29. M. C. McCarthy, C. A. Gottlieb, P. Thaddeus, S. Thorwirth and J. Gauss, *The Journal of Chemical Physics*, 2011, **134**, 034306.
30. P. Thaddeus, M. Kutner, A. Penzias, R. Wilson and K. Jefferts, *The Astrophysical Journal*, 1972, **176**, L73.
31. P. Schilke, D. Benford, T. Hunter, D. Lis and T. Phillips, *The Astrophysical Journal Supplement Series*, 2001, **132**, 281.

32. V. L. Fish, *The Astrophysical Journal Letters*, 2006, **646**, L57.
33. R. Kaiser, A. Mebel and Y. Lee, *The Journal of Chemical Physics*, 2001, **114**, 231-239.
34. X. Gu, Y. Guo and R. I. Kaiser, *International Journal of Mass Spectrometry*, 2005, **246**, 29-34.
35. Y. Guo, X. Gu, E. Kawamura and R. I. Kaiser, *Review of Scientific Instruments*, 2006, **77**, 034701.
36. N. R. Daly, *Review of Scientific Instruments*, 1960, **31**, 264-267.
37. G. O. Brink, *Review of Scientific Instruments*, 1966, **37**, 857-860.
38. D. S. Parker, A. V. Wilson, R. I. Kaiser, N. J. Mayhall, M. Head-Gordon and A. G. Tielens, *The Astrophysical Journal*, 2013, **770**, 33.
39. T. Yang, B. B. Dangi, A. M. Thomas, B. J. Sun, T. J. Chou, A. H. Chang and R. I. Kaiser, *Angewandte Chemie*, 2016, **128**, 8115-8119.
40. T. Yang, A. M. Thomas, B. B. Dangi, R. I. Kaiser, M.-H. Wu, B.-J. Sun and A. H. Chang, *The Journal of Physical Chemistry A*, 2016, **120**, 7262-7268.
41. T. Yang, A. M. Thomas, B. B. Dangi, R. I. Kaiser, A. M. Mebel and T. J. Millar, *Nature Communications*, 2018, **9**, 1-8.
42. X. Gu, Y. Guo, E. Kawamura and R. I. Kaiser, *Journal of Vacuum Science & Technology A: Vacuum, Surfaces, and Films*, 2006, **24**, 505-511.
43. W. Bauer, K. H. Becker, R. Düren, C. Hubrich and R. Meuser, *Chemical Physics Letters*, 1984, **108**, 560-561.
44. M. F. Vernon, Ph.D. Dissertation, University of California at Berkeley, 1983.
45. P. S. Weiss, Ph.D. Dissertation, University of California at Berkeley, 1985.
46. R. I. Kaiser, *Chemical Reviews*, 2002, **102**, 1309-1358.
47. R. D. Levine and R. B. Bernstein, *Molecular Reaction Dynamics and Chemical Reactivity*, Oxford University Press, USA, 1987.
48. M. W. Schmidt, K. K. Baldridge, J. A. Boatz, S. T. Elbert, M. S. Gordon, J. H. Jensen, S. Koseki, N. Matsunaga, K. A. Nguyen and S. Su, *Journal of Computational Chemistry*, 1993, **14**, 1347-1363.
49. H. Werner, P. Knowles, G. Knizia, F. Manby, M. Schütz, P. Celani, W. Györffy, D. Kats, T. Korona, R. Lindh, A. Mitrushenkov, G. Rauhut, K. Shamasundar, T. Adler, R. Amos, A. Bernhardsson, A. Berning, D. Cooper, J. Deegan, A. Dobbyn, F. Eckert, E. Goll, C. Hampel, A. Hesselmann, G. Hetzer, T. Hrenar, G. Jansen, C. Köppl, Y. Liu, A. Lloyd, R. Mata, A. May, S. McNicholas, W. Meyer, M. Mura, A. Nicklass, D. O'Neill, P. Palmieri, D. Peng, K. Pflüger, R. Pitzer, M. Reiher, T. Shiozaki, H. Stoll, A. Stone, R. Tarroni, T. Thorsteinsson and M. Wang, *Molpro, Version 2015.1, a Package of Ab Initio Programs*, University of Cardiff: Cardiff, UK, 2015, <http://www.molpro.net>.
50. W. Kohn and L. J. Sham, *Physical Review*, 1965, **140**, A1133.
51. Y. Zhao and D. G. Truhlar, *Theoretical Chemistry Accounts*, 2008, **120**, 215-241.
52. T. H. Dunning Jr., K. A. Peterson and A. K. Wilson, *The Journal of Chemical Physics*, 2001, **114**, 9244-9253.
53. T. H. Dunning Jr., *The Journal of Chemical Physics*, 1989, **90**, 1007-1023.
54. R. A. Kendall, T. H. Dunning Jr. and R. J. Harrison, *The Journal of Chemical Physics*, 1992, **96**, 6796-6806.
55. P. J. Knowles, C. Hampel and H. J. Werner, *The Journal of Chemical Physics*, 1993, **99**, 5219-5227.
56. P. J. Knowles, C. Hampel and H.-J. Werner, *The Journal of Chemical Physics*, 2000, **112**, 3106-3107.
57. T. B. Adler, G. Knizia and H.-J. Werner, *The Journal of Chemical Physics*, 2007, **127**, 221106.
58. G. Knizia, T. B. Adler and H.-J. Werner, *The Journal of Chemical Physics*, 2009, **130**, 054104.
59. J. Zhang and E. F. Valeev, *Journal of Chemical Theory and Computation*, 2012, **8**, 3175-3186.
60. L. M. Ziurys, P. Friberg and W. M. Irvine, *The Astrophysical Journal*, 1989, **343**, 201-207.
61. J. Martin-Pintado, R. Bachiller and A. Fuente, *Astronomy & Astrophysics*, 1992, **254**, 315.
62. J. Hatchell, M. Thompson, T. Millar and G. MacDonald, *Astronomy & Astrophysics Supplement Series*, 1998, **133**, 29-49.

63. J. Hatchell, G. Fuller and T. Millar, *Astronomy & Astrophysics*, 2001, **372**, 281-290.
64. A. Gusdorf, S. Cabrit, D. Flower and G. P. Des Forêts, *Astronomy & Astrophysics*, 2008, **482**, 809-829.
65. S. Doddipatla, C. He, S. Goettl, R. I. Kaiser, B. R. Galvão and T. J. Millar, *Science Advances*, 2021, In Press.
66. N. R. Crockett, E. A. Bergin, J. L. Neill, C. Favre, P. Schilke, D. C. Lis, T. A. Bell, G. Blake, J. Cernicharo and M. Emprechtinger, *The Astrophysical Journal*, 2014, **787**, 112.
67. P. N. Brown, G. D. Byrne and A. C. Hindmarsh, *SIAM Journal on Scientific and Statistical Computing*, 1989, **10**, 1038-1051.
68. E. Herbst and C. M. Leung, *The Astrophysical Journal*, 1986, **310**, 378-382.
69. D. McElroy, C. Walsh, A. Markwick, M. Cordiner, K. Smith and T. Millar, *Astronomy & Astrophysics*, 2013, **550**, A36.
70. M. A. Paiva, B. Lefloch and B. R. Galvão, *Monthly Notices of the Royal Astronomical Society*, 2020, **493**, 299-304.
71. T. Yang, B. B. Dangi, R. I. Kaiser, K. H. Chao, B. J. Sun, A. H. Chang, T. L. Nguyen and J. F. Stanton, *Angewandte Chemie International Edition*, 2017, **56**, 1264-1268.
72. Z. Yang, B.-J. Sun, C. He, S. Goettl, Y.-T. Lin, A. H. Chang and R. I. Kaiser, *The Journal of Physical Chemistry A*, 2021, **125**, 2472-2479.
73. D. Krajnovich, F. Huiken, Z. Zhang, Y. Shen and Y. Lee, *The Journal of Chemical Physics*, 1982, **77**, 5977-5989.
74. X. Gu, Y. Guo, F. Zhang and R. I. Kaiser, *The Journal of Physical Chemistry A*, 2007, **111**, 2980-2992.
75. B. Tercero, L. Vincent, J. Cernicharo, S. Viti and N. Marcelino, *Astronomy & Astrophysics*, 2011, **528**, A26.
76. F. X. Brown, S. Yamamoto and S. Saito, *Journal of Molecular Structure*, 1997, **413**, 537-544.
77. B. Tercero, J. Cernicharo, J. Pardo and J. Goicoechea, *Astronomy & Astrophysics*, 2010, **517**, A96.
78. G. Esplugues, B. Tercero, J. Cernicharo, J. Goicoechea, A. Palau, N. Marcelino and T. Bell, *Astronomy & Astrophysics*, 2013, **556**, A143.
79. G. A. Blake, E. Sutton, C. Masson and T. Phillips, *The Astrophysical Journal*, 1987, **315**, 621-645.
80. J. G. Mangum, A. Wootten, R. B. Loren and E. J. Wadiak, *The Astrophysical Journal*, 1990, **348**, 542-556.

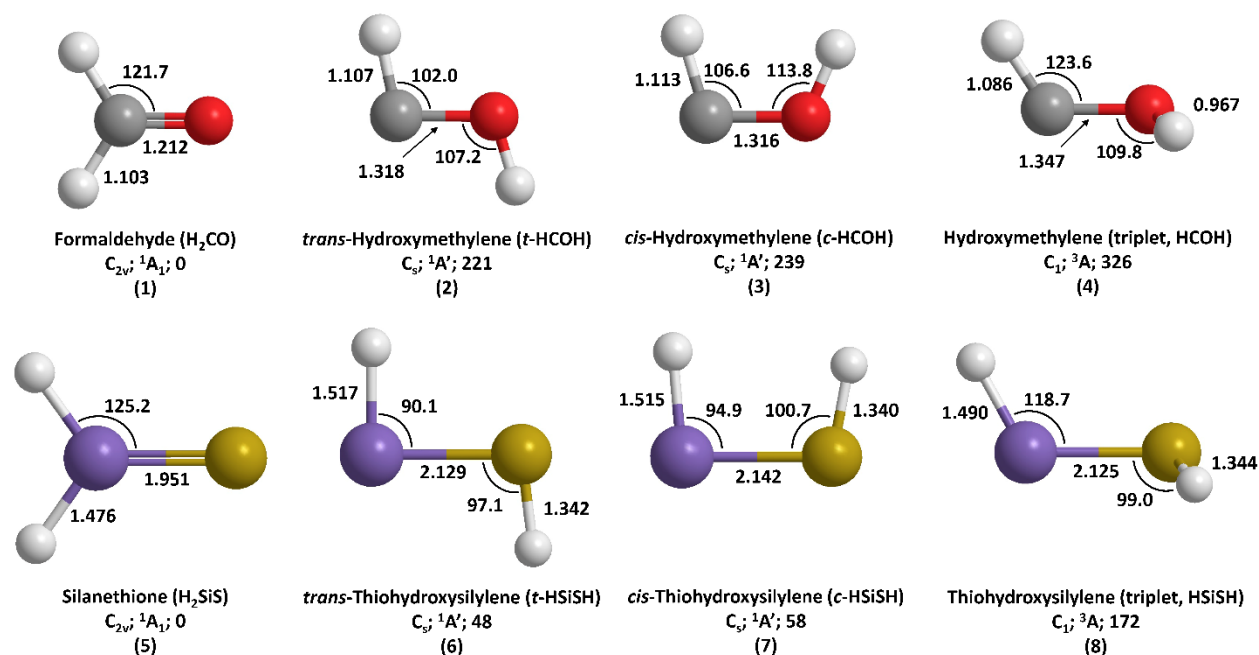


Figure 1. Geometries, bond lengths (Å), bond angles (°), point groups, electronic ground state wavefunctions, and relative energies (kJ mol⁻¹) of formaldehyde (H₂CO), silanethione (H₂SiS), and their isomers. Elements are color coded as follows: carbon (grey); oxygen (red); silicon (purple); sulfur (yellow); hydrogen (white).

Table 1. Peak velocities (v_p) and speed ratios (S) of the D1-silyldiyne (SiD; $X^2\Pi$), deuterium sulfide (D_2S ; X^1A_1), and hydrogen sulfide (H_2S ; X^1A_1) beams in addition to their collision energy (E_C) and center-of-mass angle (Θ_{CM}).

Beam	v_p (m s $^{-1}$)	S	E_C (kJ mol $^{-1}$)	Θ_{CM} ($^\circ$)
SiD ($X^2\Pi$)	1142 ± 29	6.2 ± 1.1		
D_2S (X^1A_1)	801 ± 21	12.8 ± 0.8	15.9 ± 0.9	40.8 ± 1.5
H_2S (X^1A_1)	805 ± 9	12.4 ± 0.1	15.6 ± 0.6	39.4 ± 1.0

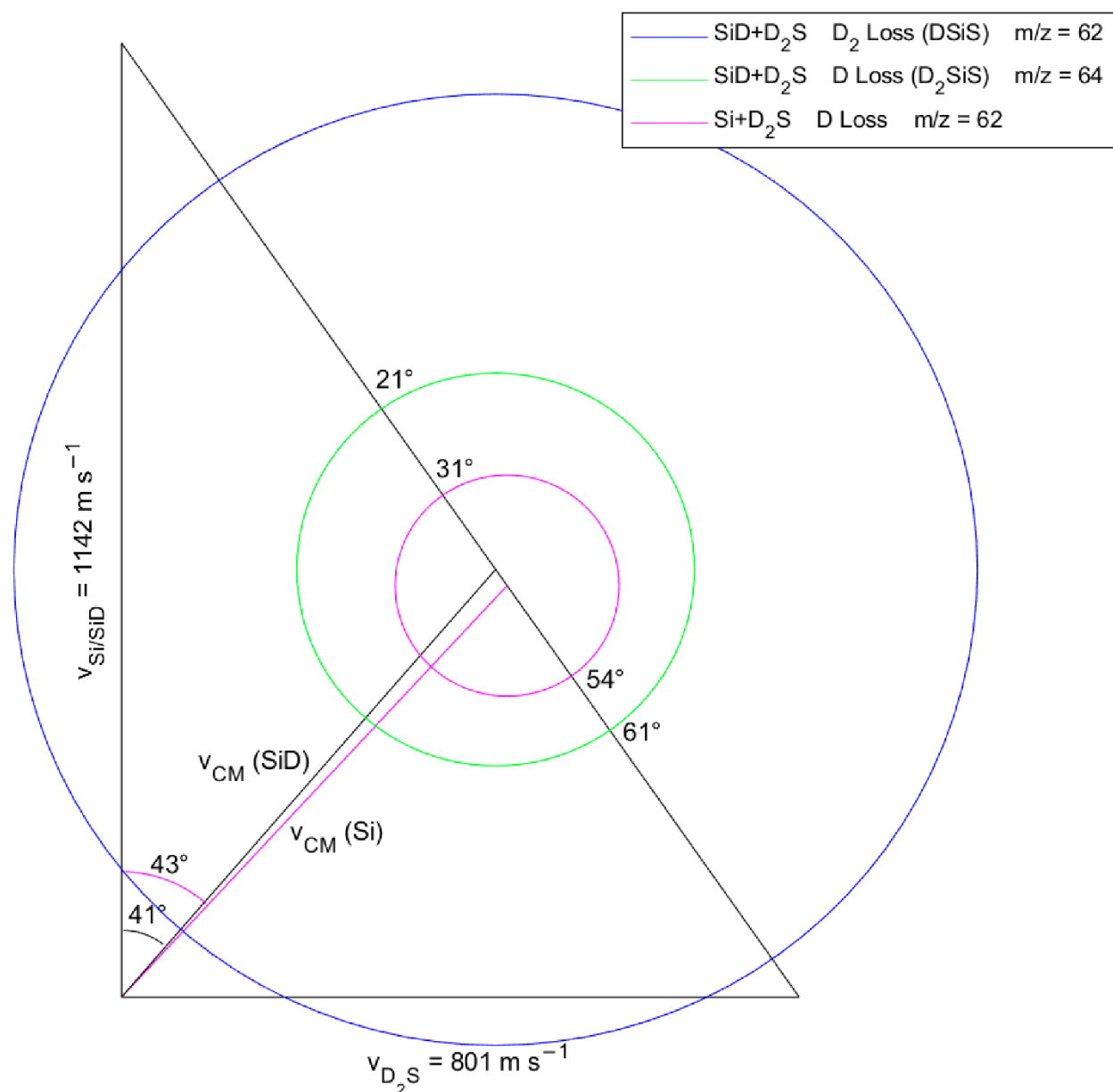


Figure 2. Newton diagram for the reaction of ground state atomic silicon ($\text{Si}(^3\text{P})$) with deuterium sulfide (D_2S) and of the D1-silyldiyne radical (SiD ; $\text{X}^2\Pi$) with deuterium sulfide (D_2S). The diagram is simplified by including only the most energetically favorable product channels for the D and D_2 loss pathways, while the full Newton diagram is shown in Figure S3. Each Newton circle has a radius equal to the maximum CM recoil velocity of its corresponding heavy product.

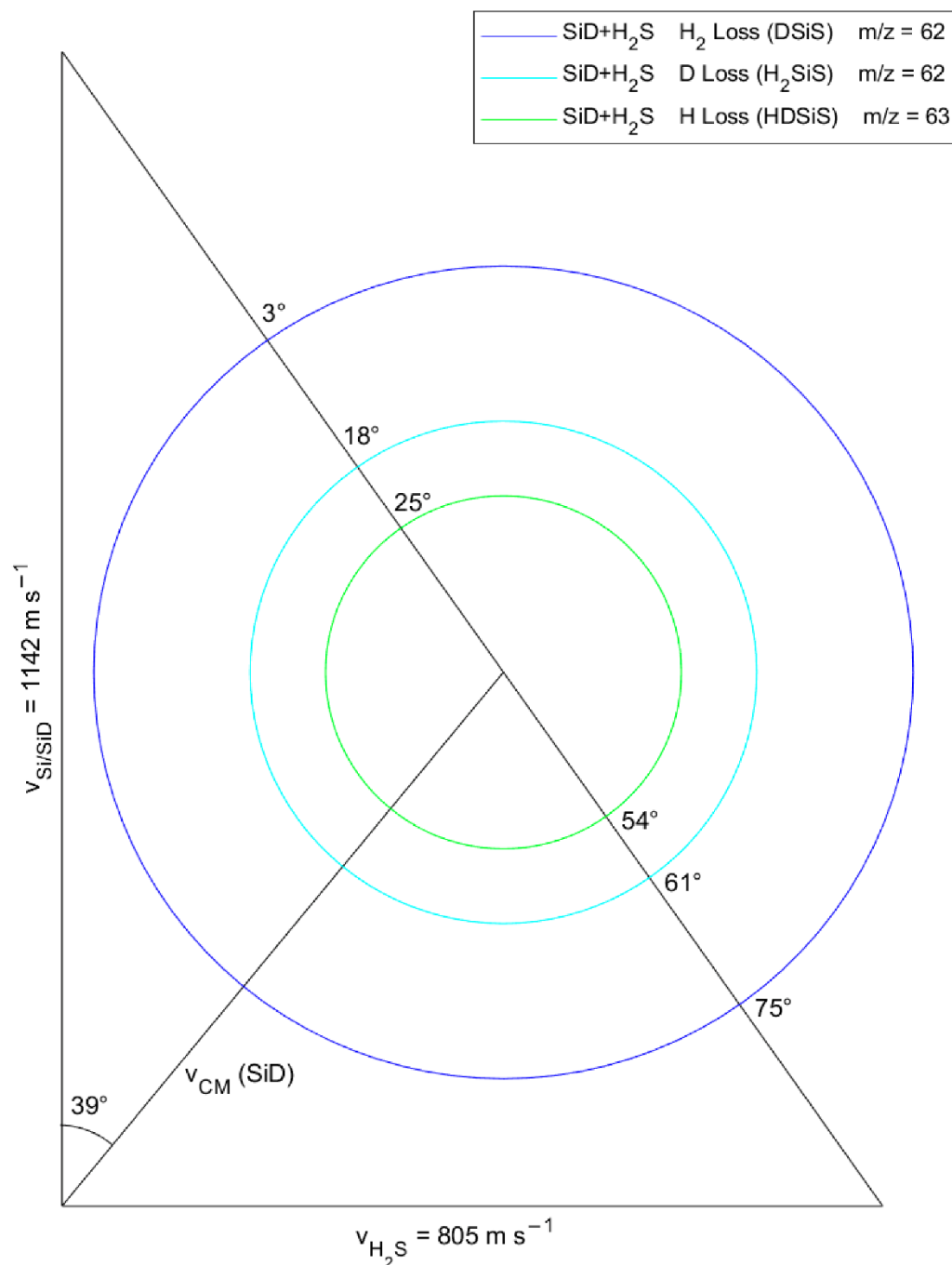


Figure 3. Newton diagram for the reaction of the D1-silylidyne radical (SiD; $X^2\Pi$) with hydrogen sulfide (H_2S). The diagram is simplified by including only the most energetically favorable products for the H, D, and H_2 loss pathways, while the full Newton diagram is shown in Figure S4. Each Newton circle has a radius equal to the maximum CM recoil velocity of its corresponding heavy product.

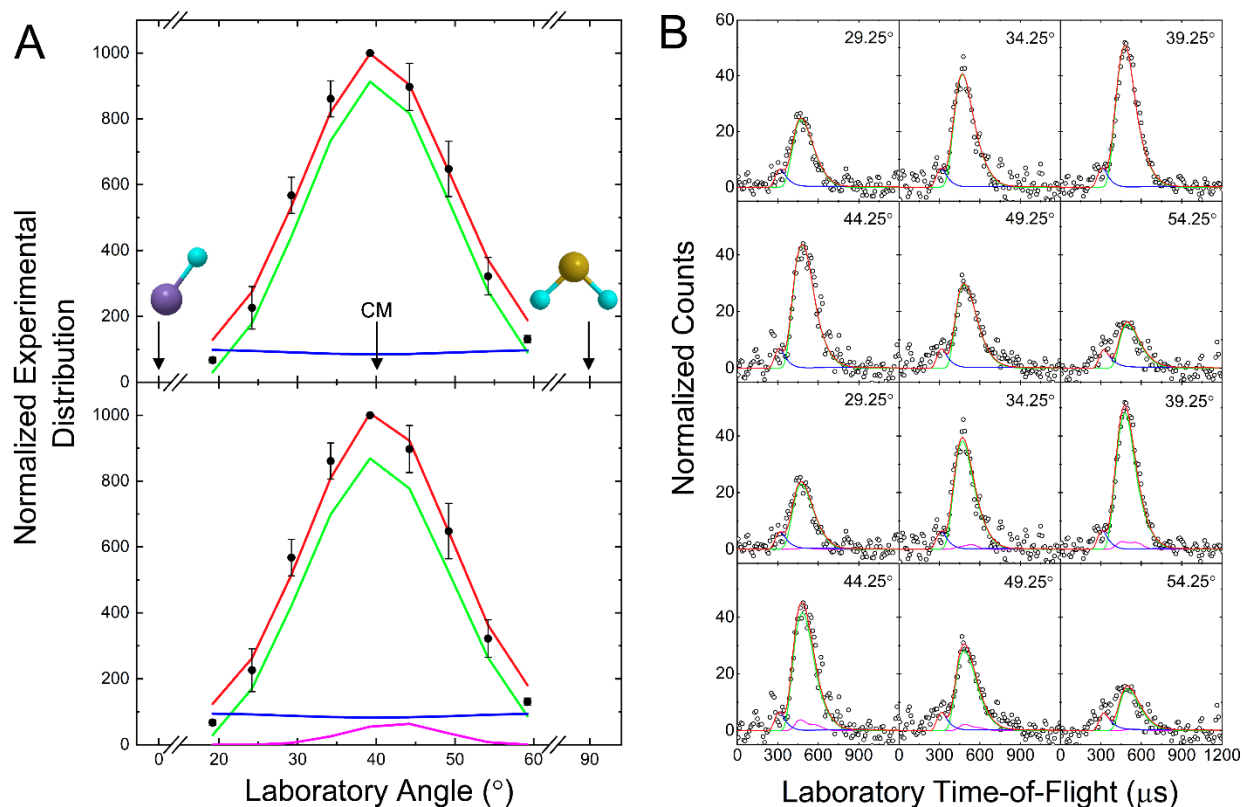


Figure 4. Laboratory angular distribution (A) and time-of-flight (TOF) spectra (B) recorded at $m/z = 62$ for the reaction of deuterium sulfide (D_2S) with the D1-silyldiyne radical (SiD ; $\text{X}^2\Pi$). The data were fit with two channels (*top*) and with three channels (*bottom*). The two channels in the *top* fits correspond to DSiS^+ at $m/z = 62$ (dark blue) and fragmentation of atomic deuterium (D) from D_2SiS^+ at $m/z = 64$ (green). The three channels in the *bottom* fits correspond to DSiS^+ at $m/z = 62$ (dark blue), fragmentation of atomic deuterium (D) from D_2SiS^+ at $m/z = 64$ (green), and also DSiS^+ at $m/z = 62$ (magenta) from the reaction of ground state atomic silicon ($\text{Si}(^3\text{P})$) with deuterium sulfide (D_2S). CM represents the center-of-mass angle, and 0° and 90° define the directions of the D1-silyldiyne and deuterium sulfide beams, respectively. The black circles depict the experimental data, colored lines the fits (red corresponding to the total fit), and error bars the 1σ standard deviation.

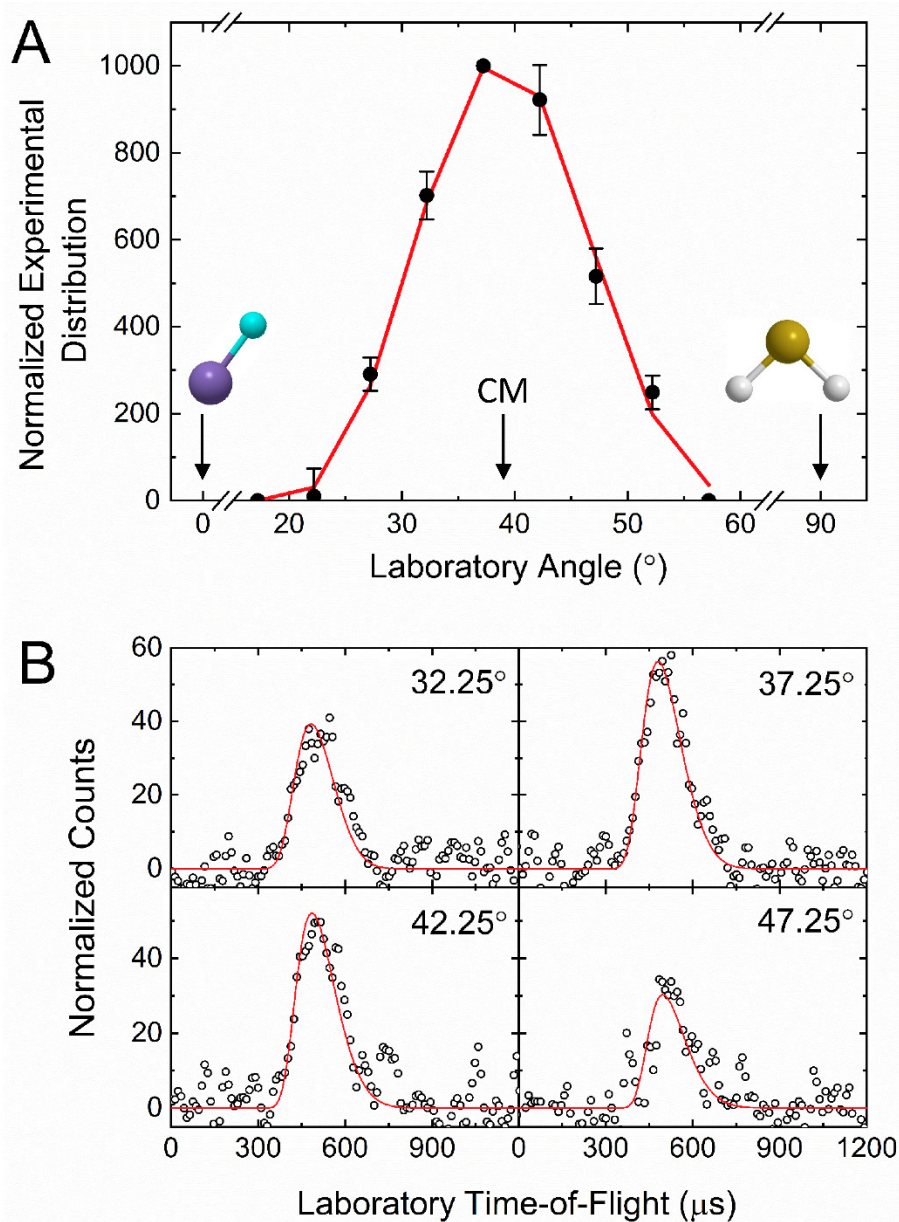


Figure 5. Laboratory angular distribution (A) and TOF spectra (B) for the reaction of hydrogen sulfide (H_2S) with the D1-silyldiyne radical (SiD ; $X^2\Pi$) recorded at $m/z = 63$, which corresponds to the ionized product HDSiS^+ . CM represents the center-of-mass angle, and 0° and 90° define the directions of the D1-silyldiyne and hydrogen sulfide beams, respectively. The black circles depict the experimental data, red lines the fit, and error bars the 1σ standard deviation.

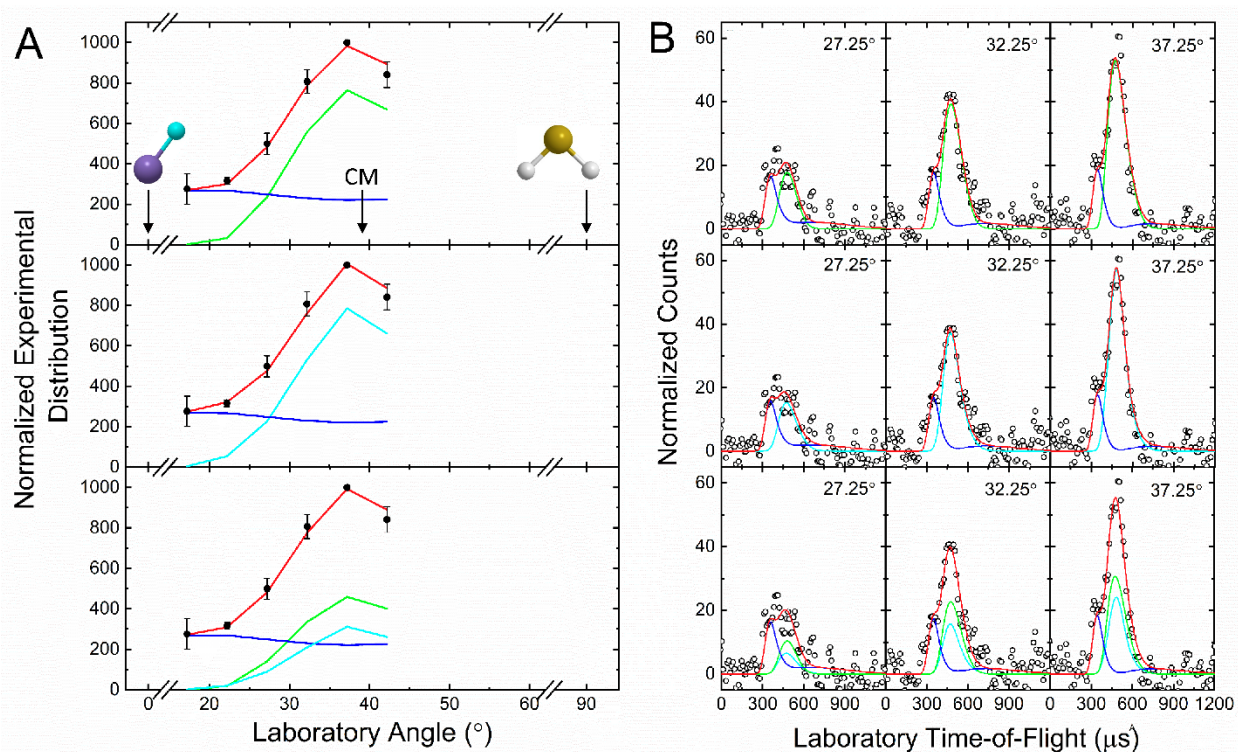


Figure 6. Laboratory angular distribution (A) and time-of-flight (TOF) spectra (B) recorded at $m/z = 62$ for the reaction of hydrogen sulfide (H_2S) with the D1-silylidyne radical (SiD ; $\text{X}^2\Pi$). There are three fits for the data: first with two channels corresponding to DSiS^+ (dark blue) at $m/z = 62$ and fragmentation of atomic hydrogen (H) from HDSiS^+ (green) at $m/z = 63$ (top); second with two channels corresponding to DSiS^+ (dark blue) at $m/z = 62$ and H_2SiS^+ (light blue) at $m/z = 62$ (middle); and third with all three channels (bottom). CM represents the center-of-mass angle, and 0 $^{\circ}$ and 90 $^{\circ}$ define the directions of the D1-silylidyne and hydrogen sulfide beams, respectively. The black circles depict the experimental data, colored lines the fits (red corresponding to the total fit), and error bars the 1 σ standard deviation.

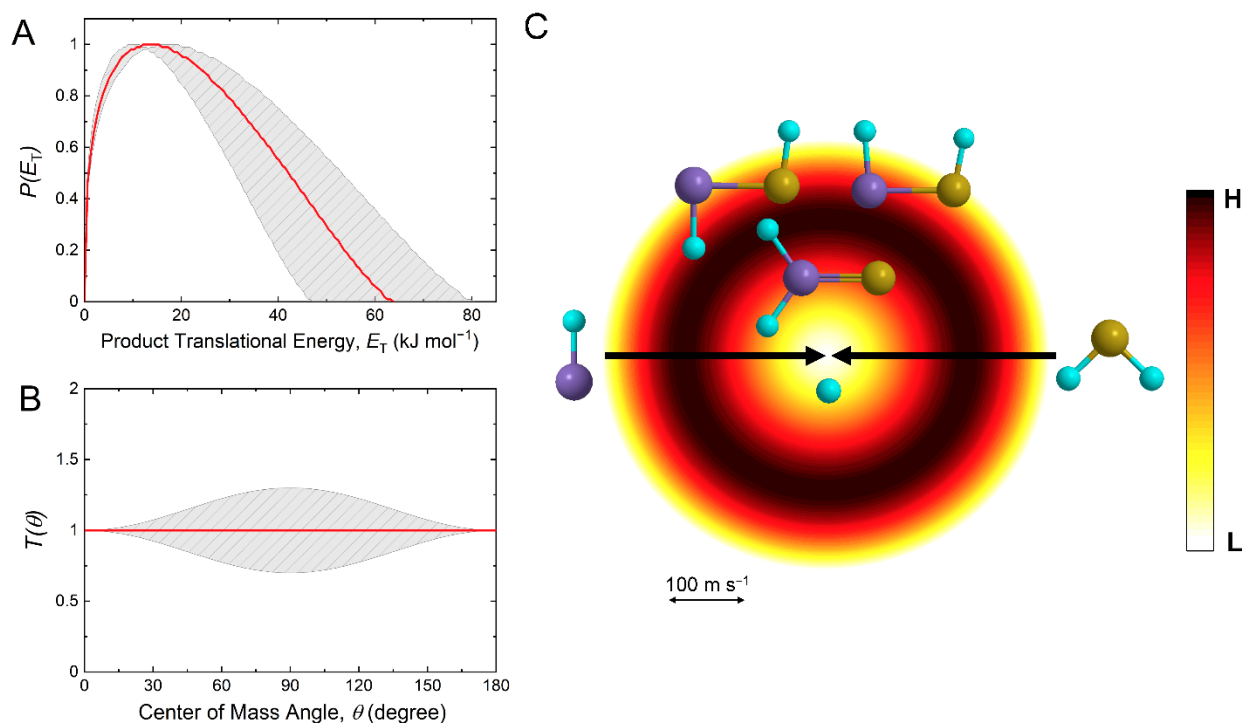


Figure 7. CM translational energy (A) and angular (B) flux distributions, as well as the associated flux contour map (C) leading to the formation of D₂SiS/DSiSD ($m/z = 64$) plus atomic deuterium in the reaction of the D1-silylidyne radical (SiD; $X^2\Pi$) with deuterium sulfide (D₂S). Red lines define the best-fit functions while shaded areas denote the error limits. The flux contour map represents the flux intensity of the reactively scattered products as a function of the product velocity (u) and CM scattering angle (θ), and the color bar indicates the flux gradient from high (H) to low (L) intensity. Atoms are colored as follows: silicon (purple); sulfur (yellow); deuterium (light blue).

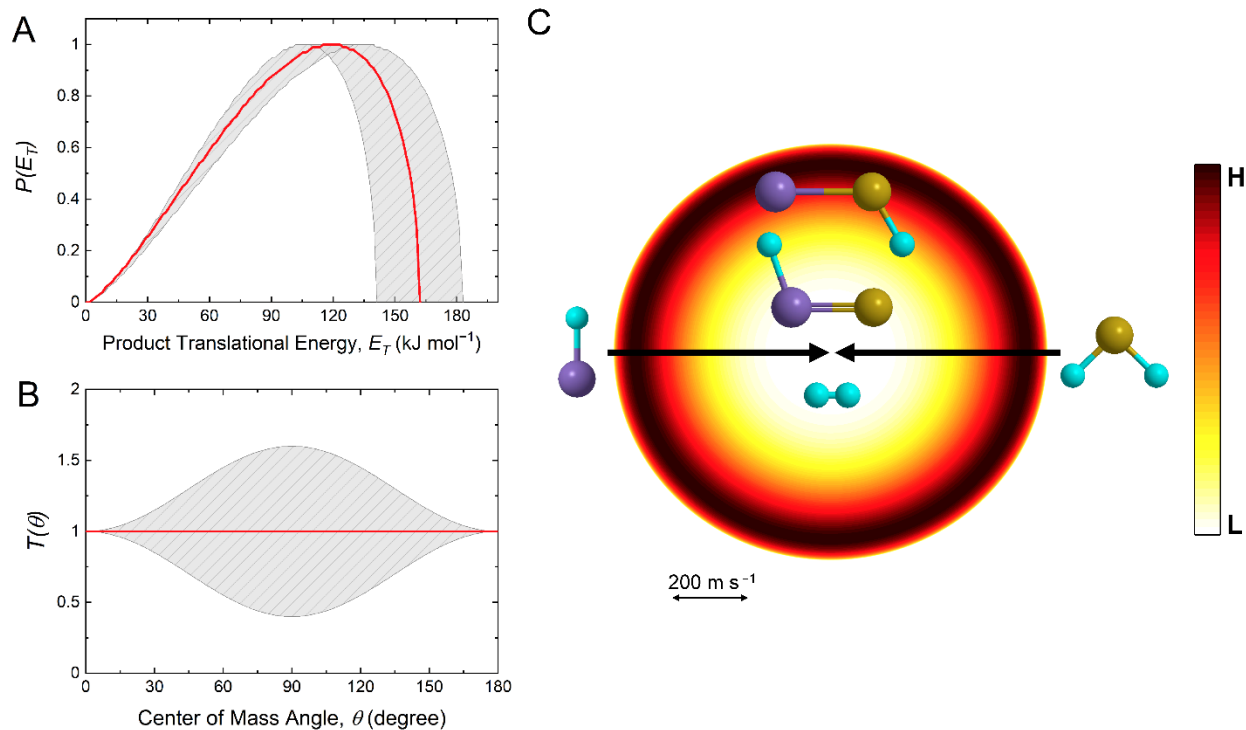


Figure 8. CM translational energy (A) and angular (B) flux distributions, as well as the associated flux contour map (C) leading to the formation of the D1-(iso)thiosilaformyl (DSiS/SiSD) radical ($m/z = 62$) plus molecular deuterium in the reaction of D1-silyldiyne radical (SiD; $X^2\Pi$) with deuterium sulfide (D_2S). Red lines define the best-fit functions while shaded areas denote the error limits. The flux contour map represents the flux intensity of the reactively scattered products as a function of the product velocity (u) and CM scattering angle (θ), and the color bar indicates the flux gradient from high (H) to low (L) intensity. Atoms are colored as follows: silicon (purple); sulfur (yellow); deuterium (light blue)

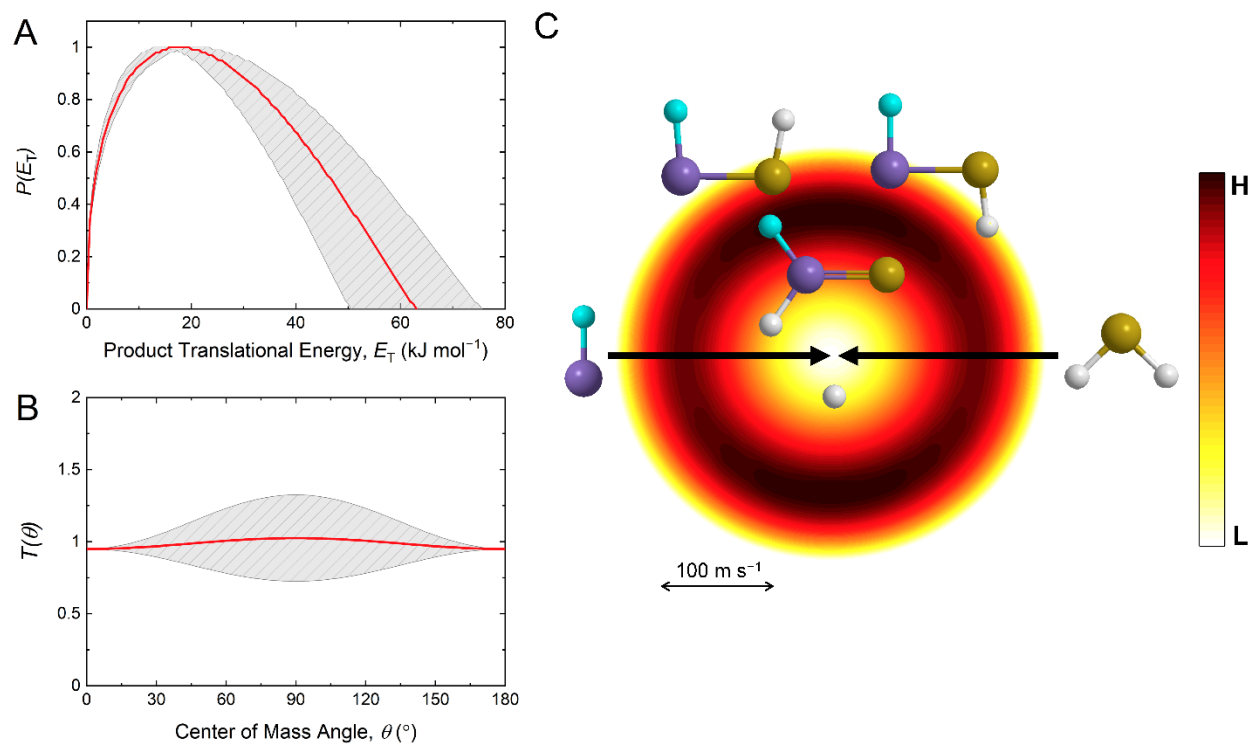


Figure 9. CM translational energy (A) and angular (B) flux distributions, as well as the associated flux contour map (C) leading to the formation of D1-silanethione (HDSiS) and *trans/cis*-D1-thiohydroxysilylene (DSiSH/HSiSD) molecules ($m/z = 63$) plus atomic hydrogen in the reaction of D1-silyldiyne radical (SiD; $X^2\Pi$) with hydrogen sulfide (H_2S). Red lines define the best-fit functions while shaded areas denote the error limits. The flux contour map represents the flux intensity of the reactively scattered products as a function of the product velocity (u) and CM scattering angle (θ), and the color bar indicates the flux gradient from high (H) to low (L) intensity. Atoms are colored as follows: silicon (purple); sulfur (yellow); deuterium (light blue); hydrogen (white).

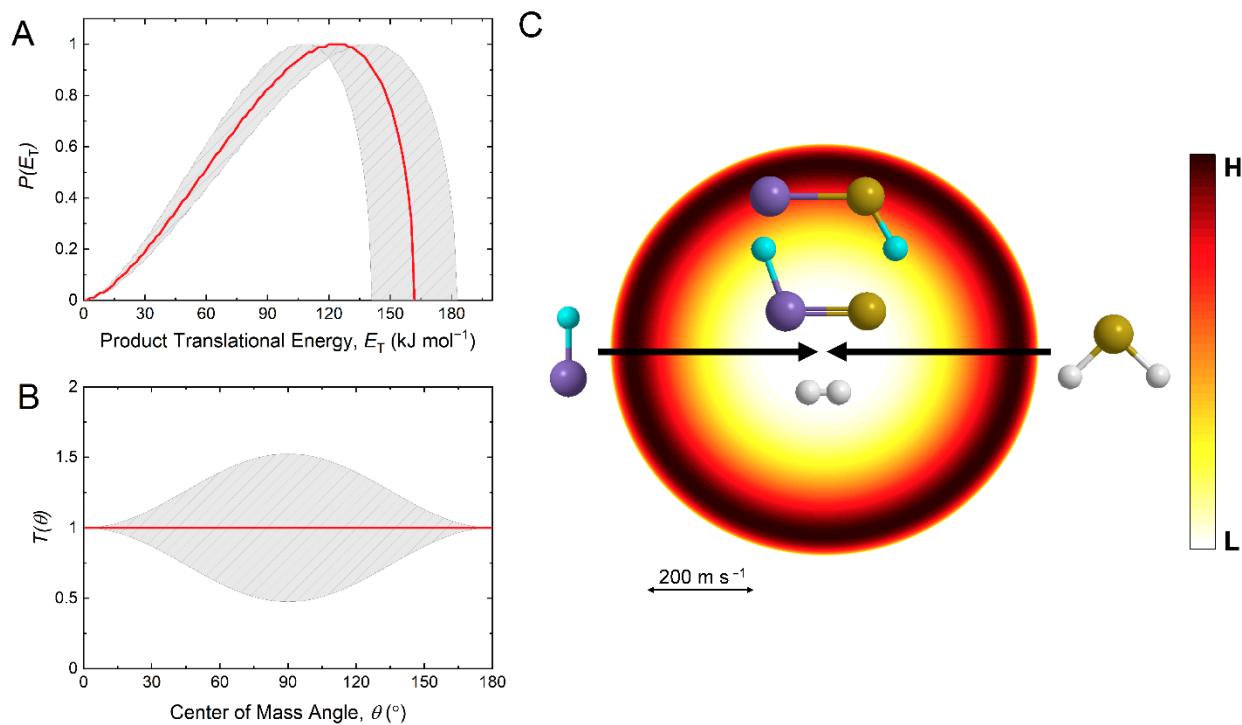


Figure 10. CM translational energy (A) and angular (B) flux distributions, as well as the associated flux contour map (C) leading to the formation of the D1-(iso)thiosilaformyl (DSiS/SiSD) radical ($m/z = 62$) plus molecular hydrogen in the reaction of D1-silyldiyne radical (SiD; $X^2\Pi$) with hydrogen sulfide (H_2S). Red lines define the best-fit functions while shaded areas denote the error limits. The flux contour map represents the flux intensity of the reactively scattered products as a function of the product velocity (u) and CM scattering angle (θ), and the color bar indicates the flux gradient from high (H) to low (L) intensity. Atoms are colored as follows: silicon (purple); sulfur (yellow); deuterium (light blue); hydrogen (white).

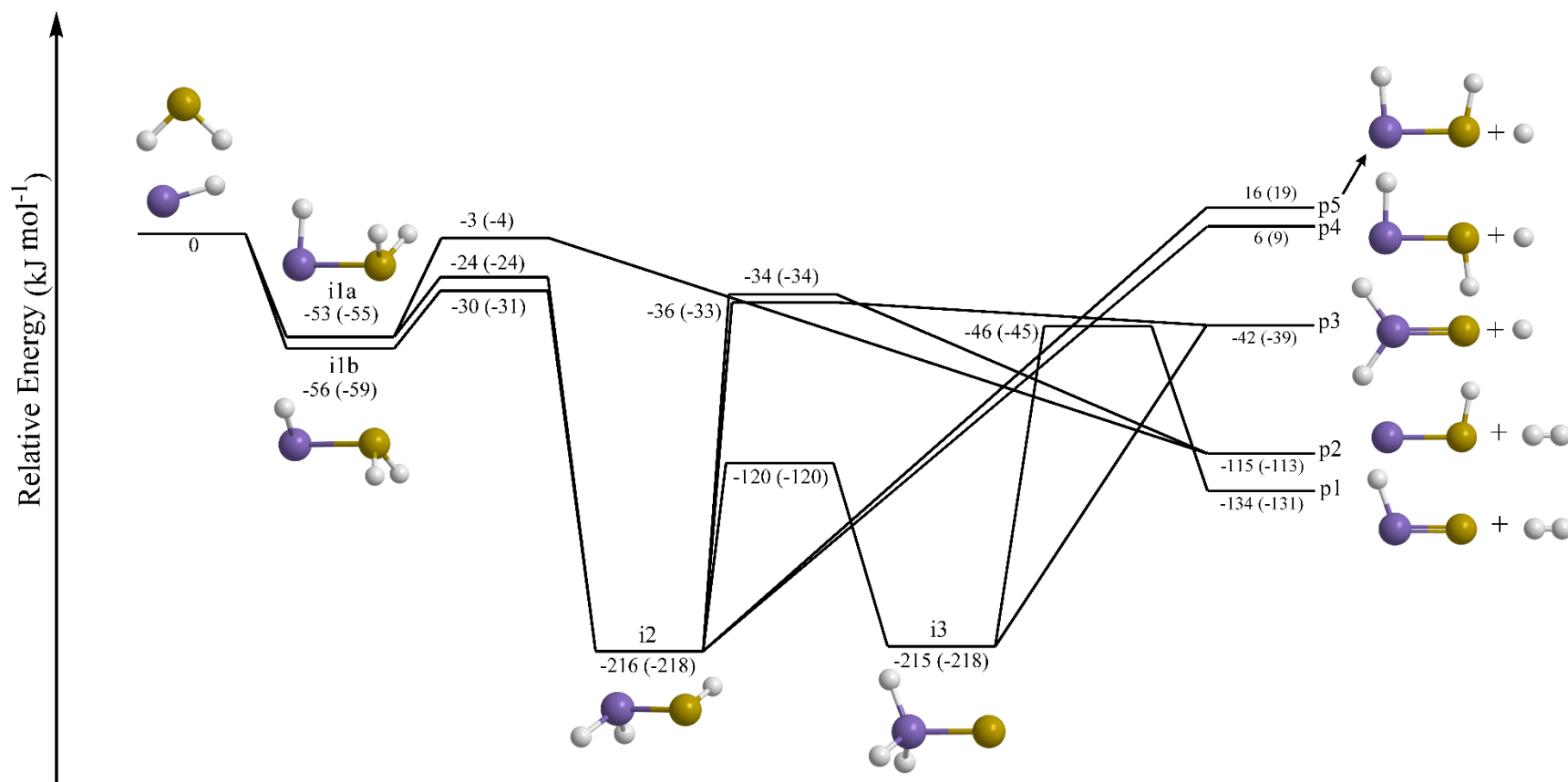


Figure 11. Potential energy surface for the reaction of the silyldiyne radical ($\text{SiH}; \text{X}^2\Pi$) with hydrogen sulfide (H_2S). Relative energies calculated at the CCSD(T)-F12/aug-cc-pV(T+d)Z//CCSD(T)/aug-cc-pV(T+d)Z+ZPE(M06-2X/cc-pV(T+d)Z) level of theory are shown in kJ mol^{-1} , with calculations for the fully deuterated system shown in parentheses. The surface is simplified by removing barriers, intermediates, and most products above the collision energy of 15.6 kJ mol^{-1} . Atoms are colored as follows: silicon (purple); sulfur (yellow); hydrogen (white).

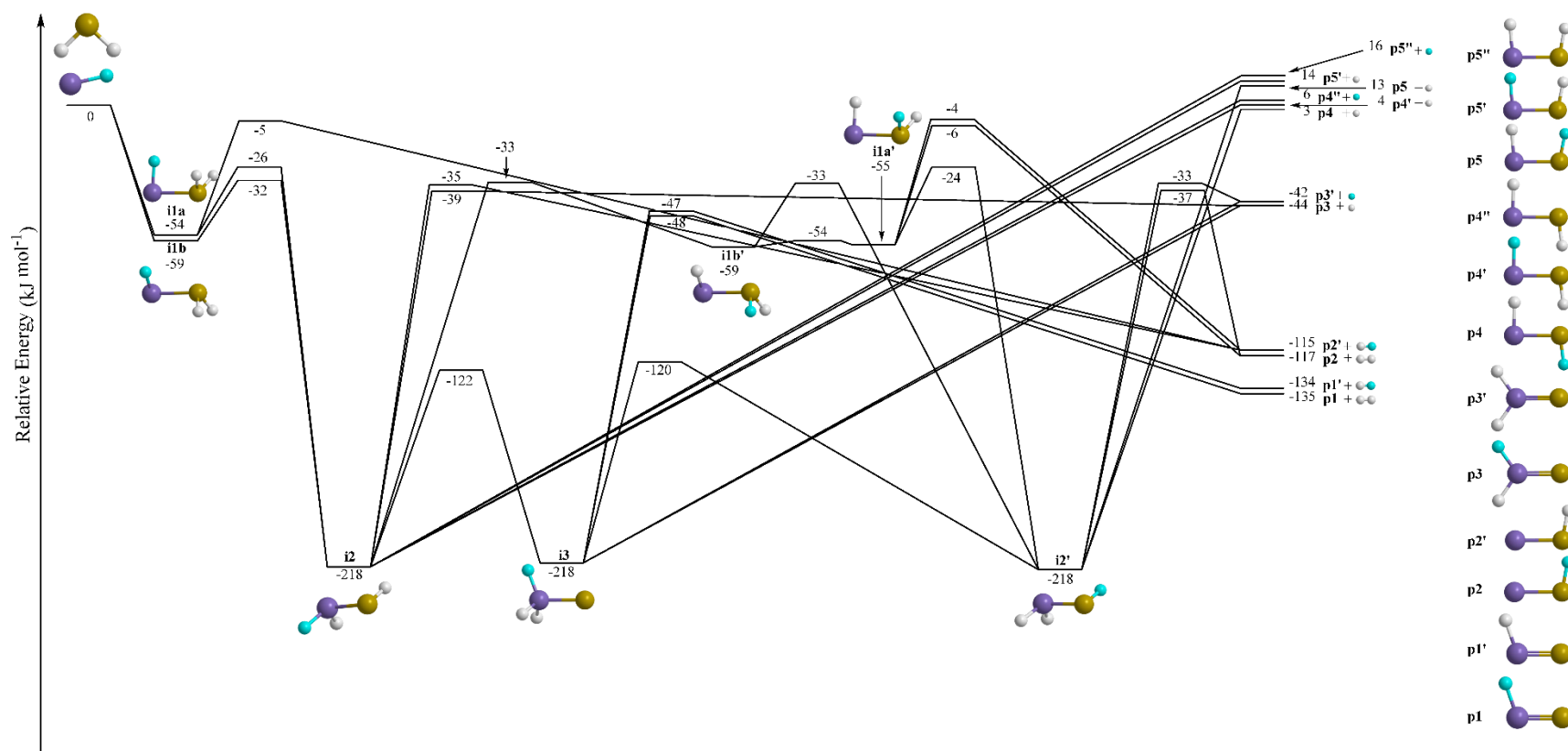


Figure 12. Potential energy surface for the reaction of the D1-silyldiyne radical (SiD; $X^2\Pi$) with hydrogen sulfide (H_2S). Relative energies calculated at the CCSD(T)-F12/aug-cc-pV(T+d)Z//CCSD(T)/aug-cc-pV(T+d)Z+ZPE(M06-2X/cc-pV(T+d)Z) level of theory are shown in kJ mol^{-1} . The surface is simplified by removing barriers, intermediates, and most products above the collision energy of 15.6 kJ mol^{-1} . Atoms are colored as follows: silicon (purple); sulfur (yellow); hydrogen (white); deuterium (light blue).

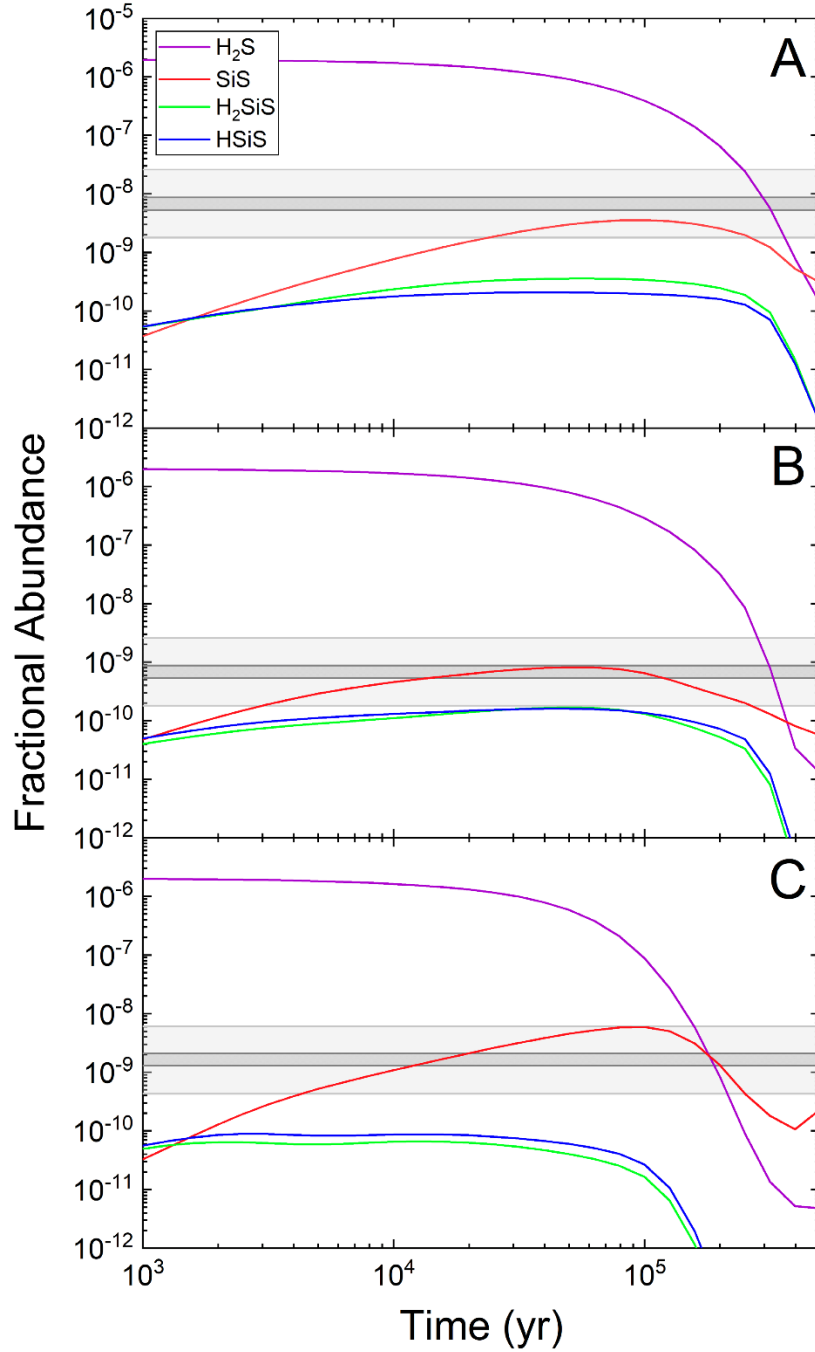


Figure 13. Time-dependent evolution of the abundances of H_2S , SiS , H_2SiS , and HSiS relative to H_2 in the Orion 15.5 km s^{-1} component (A), Orion Hot Core (B), and Orion Plateau (C) at densities of $n(\text{H}_2) = 5 \times 10^5 \text{ cm}^{-3}$, $5 \times 10^7 \text{ cm}^{-3}$, and $1 \times 10^6 \text{ cm}^{-3}$, and temperatures of 200 K, 225 K, and 125 K, respectively. The grey areas show observed fractional abundances of SiS , with the light grey designating a larger error range for $\text{N}(\text{H}_2)$.

Supplementary Information for

Chemical Dynamics Study on the Gas-Phase Reaction of the D1-Silyldyne Radical (SiD; X²Π) with Deuterium Sulfide (D₂S) and Hydrogen Sulfide (H₂S)

Shane J. Goettl,^a Srinivas Doddipatla,^a Zhenghai Yang,^a Chao He,^a Ralf I. Kaiser^{a,*}

^a *Department of Chemistry, University of Hawai'i at Manoa, Honolulu, Hawaii 96822, USA*

Corresponding Author: ralfk@hawaii.edu

Mateus Xavier Silva,^b Breno R. L. Galvão^{b,*}

^b *Centro Federal de Educação Tecnológica de Minas Gerais, CEFET-MG, Av. Amazonas 5253, 30421-169 Belo Horizonte, Minas Gerais, Brazil*

Corresponding Author: brenogalvao@gmail.com

Tom J. Millar^{c,*}

^c *School of Maths and Physics, Queen's University Belfast, University Road, Belfast BT7 1NN, Northern Ireland*

Corresponding Author: Tom.Millar@qub.ac.uk

Supplementary Note 1. Pulse Sequence.

An optimized pulse sequence (Figure S1) was used to coordinate the data collection. A 17.0 ± 0.1 cm diameter, four-slot (0.76 ± 0.01 mm) chopper wheel rotating at 120 Hz provided with an infrared photodiode pulse initiated the trigger ($T_0 = 0$ μ s) for the synchronization of the equipment. The photodiode sent a 480 Hz signal that was divided to 60 Hz and conveyed to three pulse/delay generators (PDG I-III; DG535, Stanford Research Systems). For the SiD/D₂S reaction, the PDG I outputs (+4 V, 50 Ω) AB ($A_I = T_0 + 1859$ μ s, $B_I = A_I + 80$ μ s) and CD ($C_I = A_I - 22$ μ s, $D_I = C_I + 80$ μ s) were sent through a pulse shaper and pulse amplifier (E-421, Physik Instrumente) and were received by the primary and secondary Proch-Trickl¹ pulsed valves, which each contain a piezoelectric disk translator (P-286.23, Physik Instrumente). This allows for a pulsed valve open time of 80 μ s when operating at an amplitude of -400 V. The output from PDG I A (TTL, high impedance) was divided to 30 Hz and directed to PDG II and III, which were used for background subtraction. PDG II AB ($A_{II} = A_I + 16654$ μ s, $B_{II} = A_{II} + 5$ μ s) and CD ($C_{II} = A_{II} + 186$ μ s, $D_{II} = C_{II} + 5$) triggered the flashlamps and Q-switch, respectively, of a neodymium-doped yttrium aluminum garnet (Nd:YAG) laser (Quanta-Ray Pro 270, Spectra-Physics) and PDG III AB ($A_{III} = A_I + 16666.66$ μ s, $B_{III} = A_{III} + 5$ μ s) triggered the MCS. For the SiD/H₂S reaction, the delay times were as follows: PDG I AB ($A_I = T_0 + 1868$ μ s, $B_I = A_I + 80$ μ s) and CD ($C_I = A_I - 22$ μ s, $D_I = C_I + 80$ μ s); PDG II AB ($A_{II} = A_I + 16643$ μ s, $B_{II} = A_{II} + 5$ μ s) and CD ($C_{II} = A_{II} + 186$ μ s, $D_{II} = C_{II} + 5$); PDG III AB ($A_{III} = A_I + 16666.66$ μ s, $B_{III} = A_{III} + 5$ μ s).

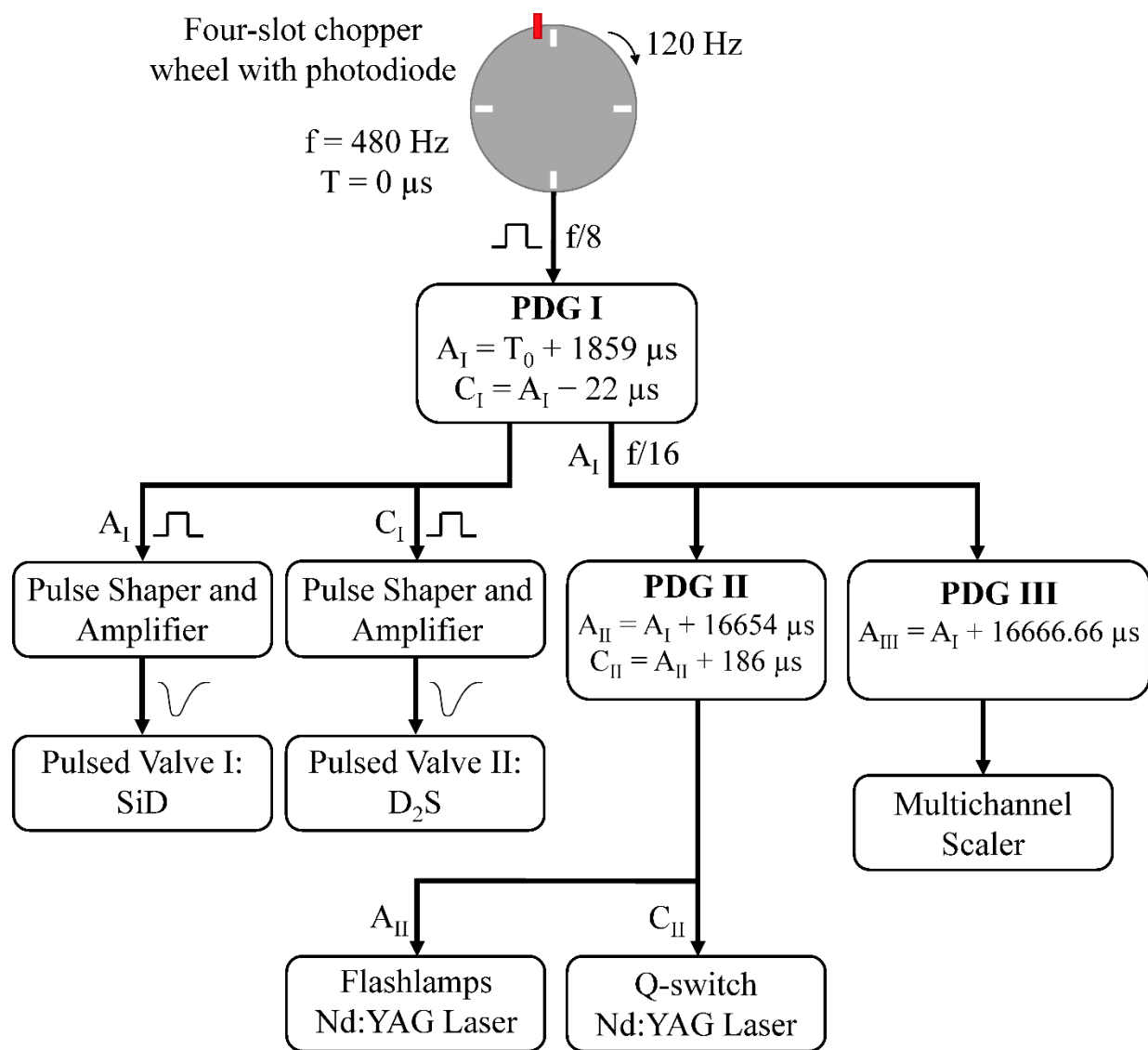


Figure S1. Pulse sequence for the crossed molecular beam reaction of the D1-silylidyne radical (SiD; $X^2\Pi$) with deuterium sulfide (D₂S) and hydrogen sulfide (H₂S).

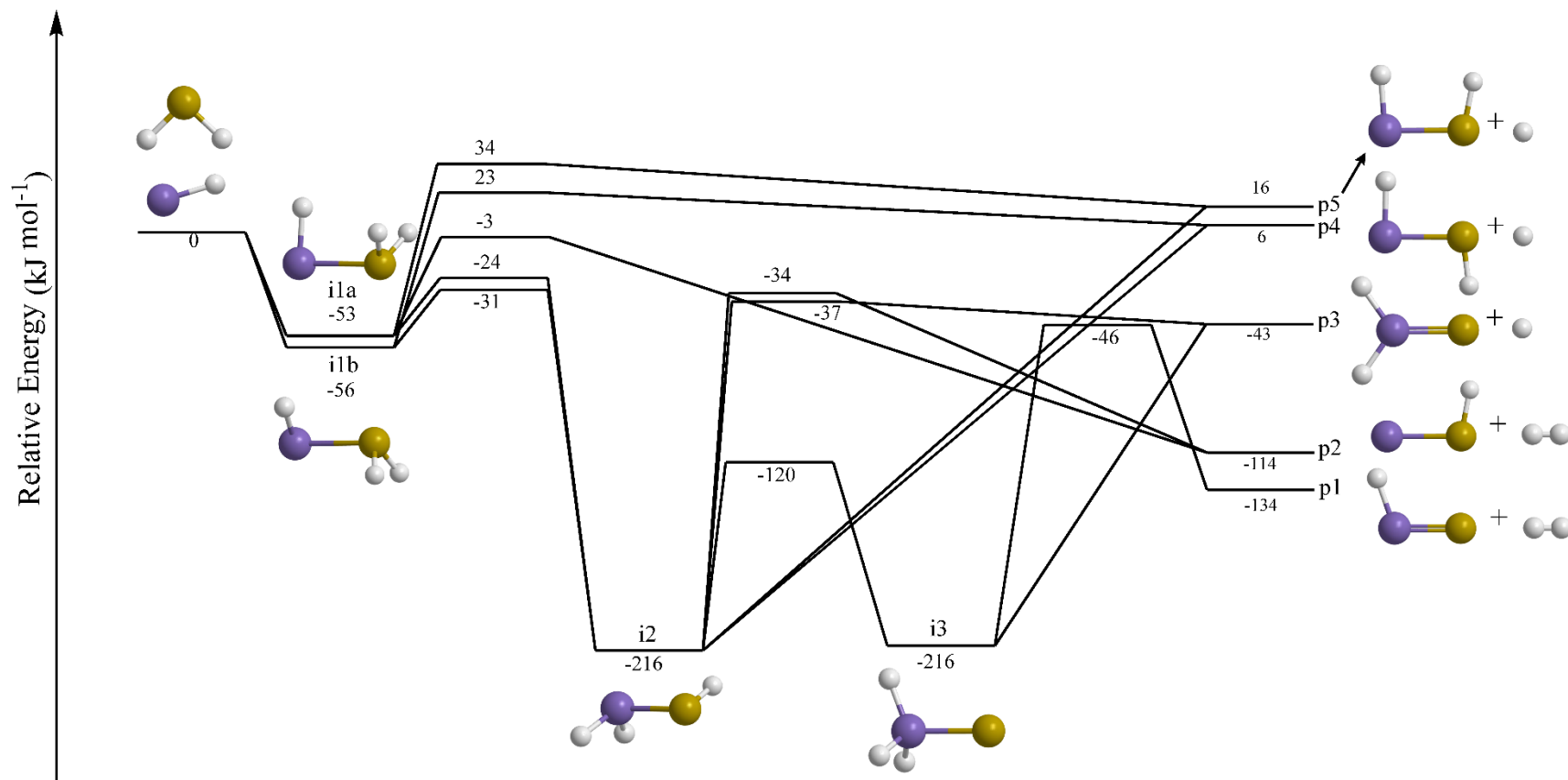


Figure S2. Schematic representation of the potential energy surface at the CCSD(T)-F12/aug-cc-pV(T+d)Z//CCSD(T)/aug-cc-pV(T+d)Z+ZPE(CCSD(T)/aug-cc-pV(T+d)Z) level for the non-deuterated ($\text{H}_2\text{S}+\text{SiH}_4$) case including transition states not accessible in our experiments.

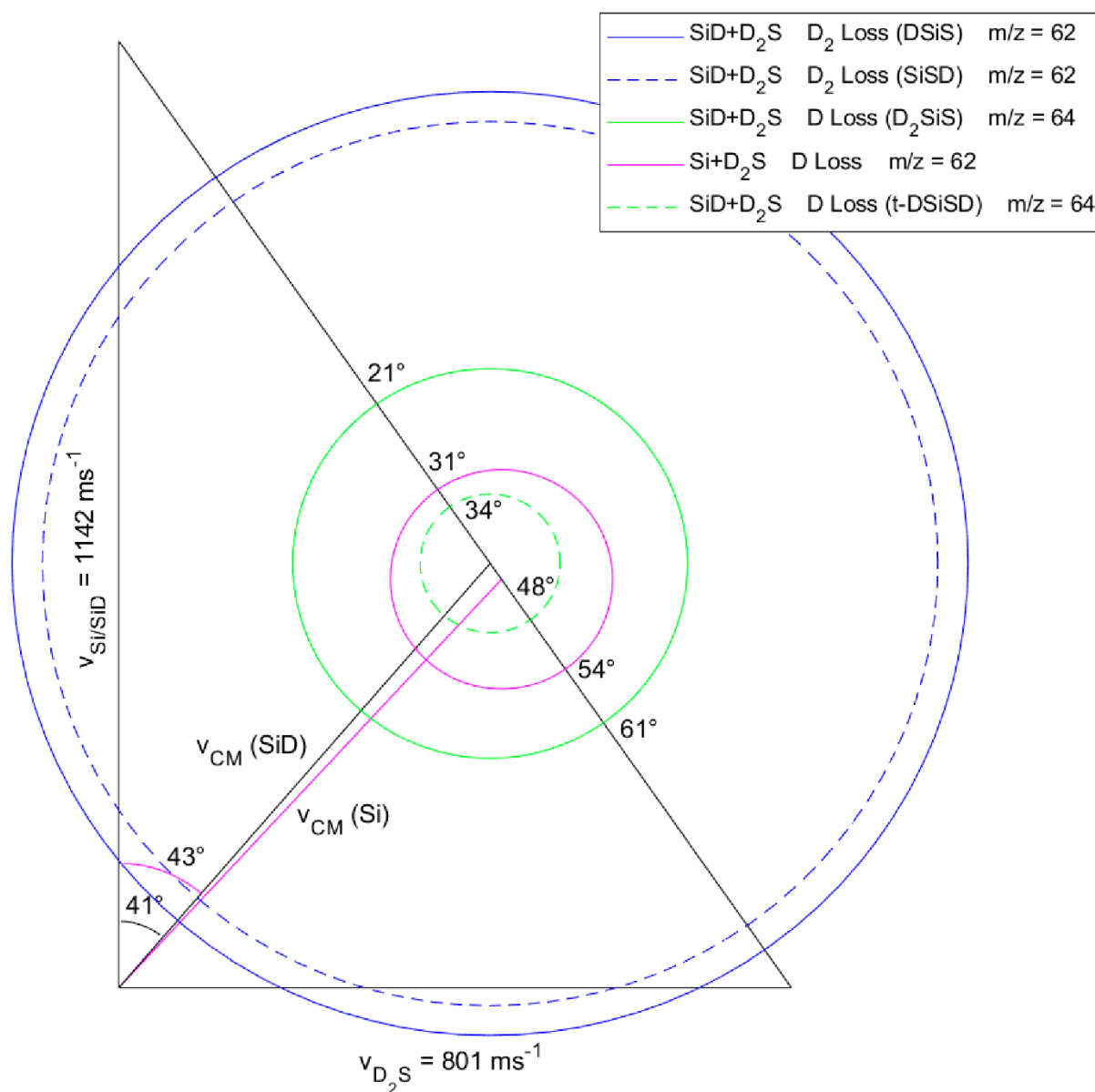


Figure S3. Newton circle diagram for the reaction of ground state atomic silicon ($\text{Si}(^3\text{P})$) with deuterium sulfide (D_2S) and of the D1-silyldyne radical (SiD ; $\text{X}^2\Pi$) with deuterium sulfide (D_2S). The diagram incorporates all reaction pathways below the reaction collision energy of 15.9 kJ mol^{-1} . Each Newton circle has a radius equal to the maximum CM recoil velocity of its corresponding heavy product, and a maximum laboratory angular scattering range for observation of products by the detector.

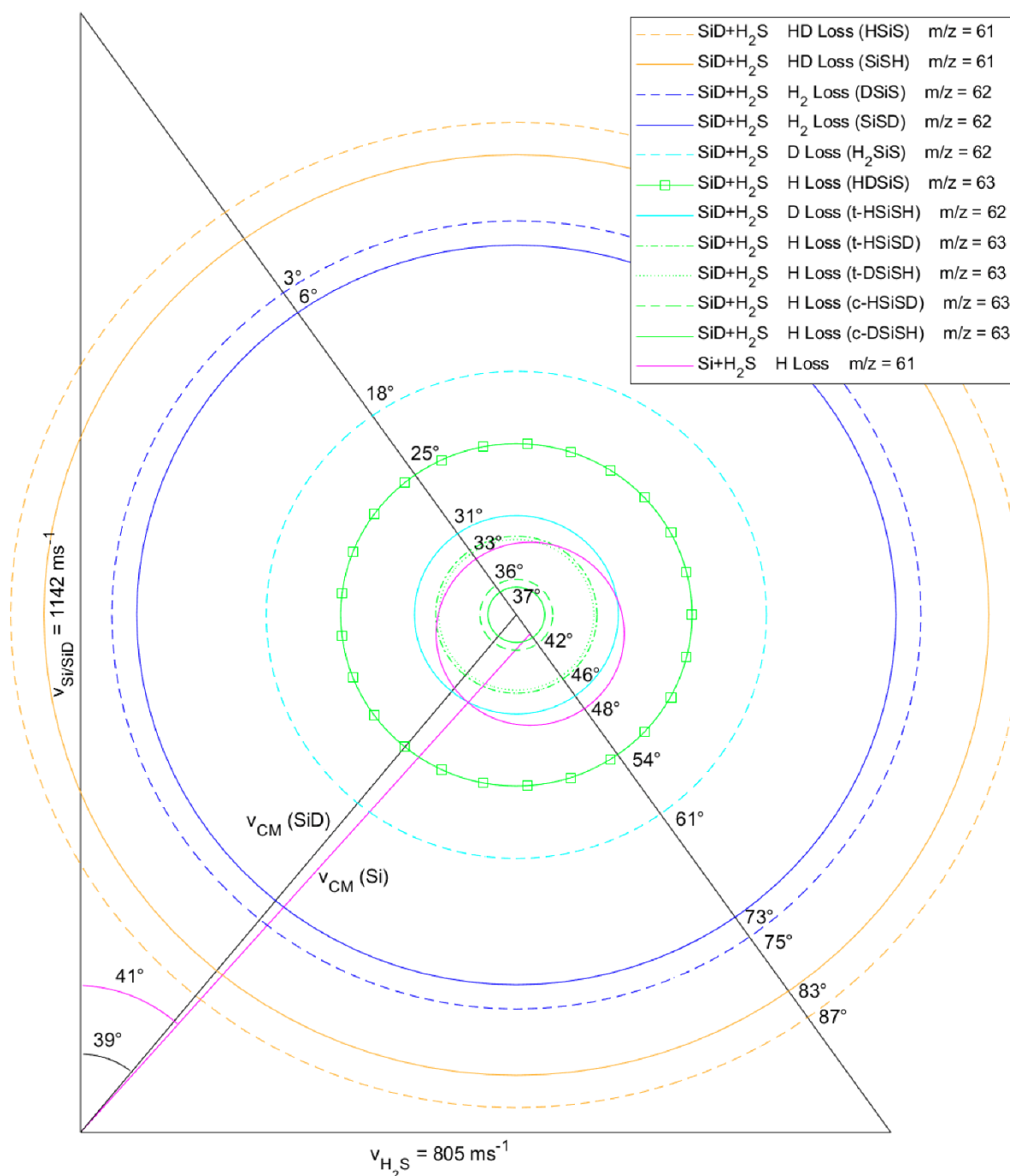


Figure S4. Newton circle diagram for the reaction of ground state atomic silicon ($\text{Si}(^3\text{P})$) with hydrogen sulfide (H_2S) and of D1-silyldyne radical (SiD ; $X^2\Pi$) with hydrogen sulfide (H_2S). The diagram incorporates all reaction pathways below the reaction collision energy of 15.6 kJ mol^{-1} . Each Newton circle has a radius equal to the maximum CM recoil velocity of its corresponding heavy product, and a maximum laboratory angular scattering range for observation of products by the detector.

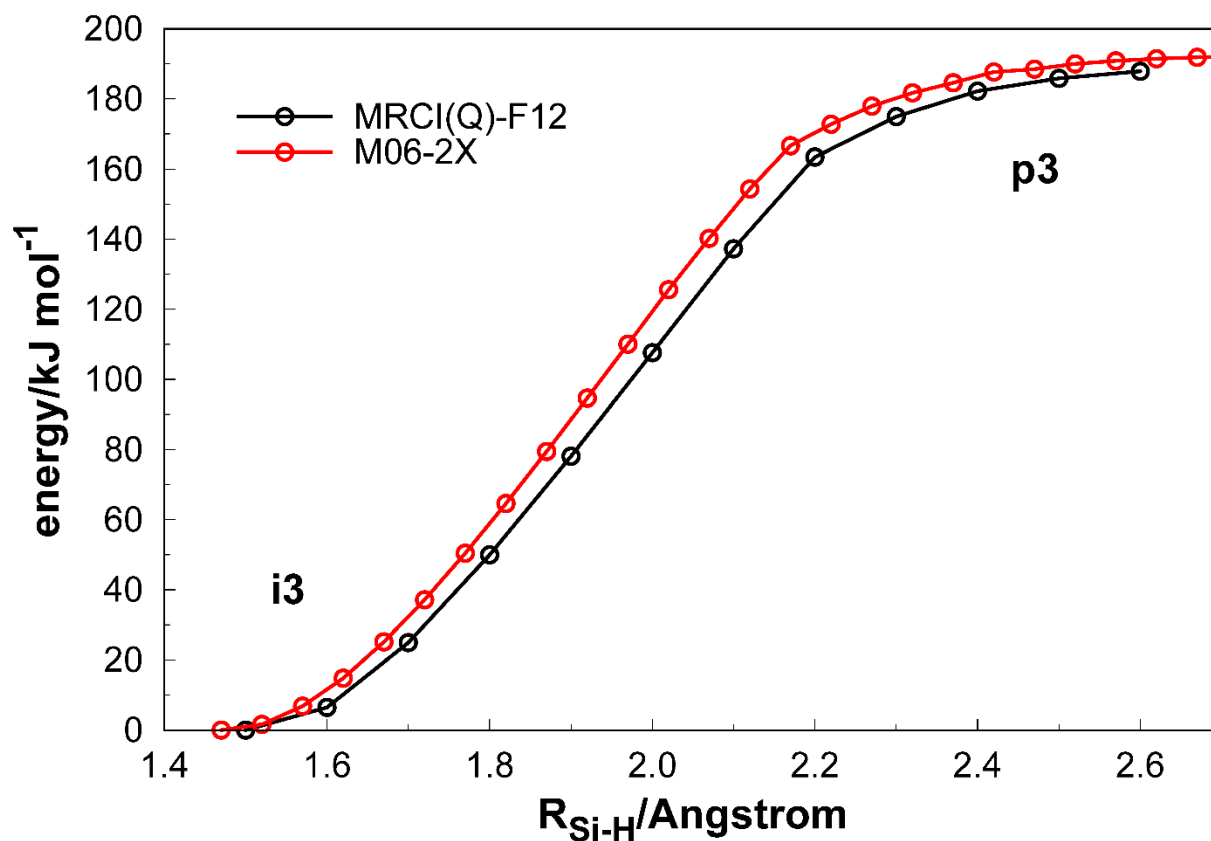


Figure S5. Optimized potential energy profile as a function of the Si-H bond for a hydrogen loss from **i3** to **p3**. To confirm the barrierless nature of this path obtained by the exploratory M06-2X/cc-pV(T+d)Z calculations (red line), a full valence CASSCF/cc-pV(T+d)Z optimization followed by single point energy refinement at the MRCI(Q)-F12 level² (black line) were performed. The energies are relative to the **i3** optimized structure for each method.

Table S1. Optimized Cartesian coordinates (Å) and vibrational frequencies (cm⁻¹) for all intermediates, transition states, reactants, and products involved in the SiH+H₂S reaction at the CCSD(T)/aug-cc-pV(T+d)Z level. The energies are given for all isotopic substitutions considered in this work at the CCSD(T)-F12/aug-cc-pV(T+d)Z//CCSD(T)/aug-cc-pV(T+d)Z+ZPE(M06-2X/cc-pV(T+d)Z) level in kJ mol⁻¹.



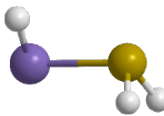
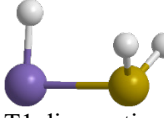
E(D0) – gives the energy of the non-deuterated case

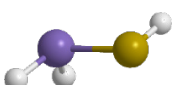


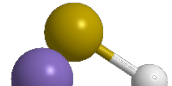

E(D1) – gives the energy for one deuterium at the first position of the Cartesian coordinates

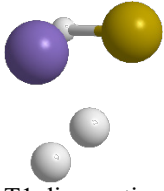
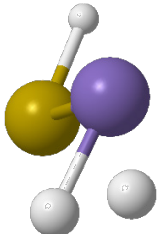
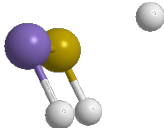
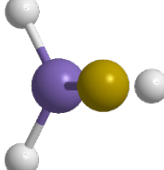
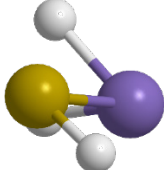
E(D2) – gives the energy for one deuterium at the second position of the Cartesian coordinates

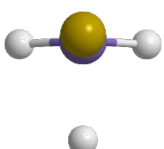
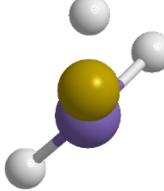
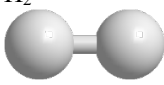
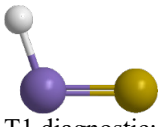
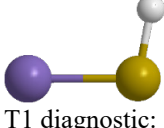
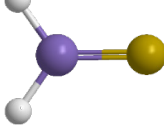
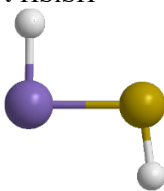
E(D3) – gives the energy for one deuterium at the third position of the Cartesian coordinates

E(D1,D2,D3) – gives the energy of the fully deuterated case

Species	Vibrational Frequencies (cm ⁻¹)	Relative Energy (kJ mol ⁻¹)	Cartesian Coordinates (Å)			
			Atom	X	Y	Z
SiH  T1 diagnostic: 0.01362941	2027.38		H	0.0000000000	0.0000000000	-0.7626723064
			Si	0.0000000000	0.0000000000	0.7626723064
H ₂ S  T1 diagnostic: 0.01105045	1211.38 2715.39 2730.68		H	0.1196696836	0.0000000000	1.2667032628
			H	1.2341510522	0.0000000000	-0.3094033975
			S	-0.0810267358	0.0000000000	-0.0572948654
i1b: HSiSH ₂  T1 diagnostic: 0.01489830	174.21 238.94 446.28 468.34 796.91 1208.04 1999.73 2652.97 2702.15	E(D0)=-55.8 E(D1)=-58.9 E(D2)=-57.1 E(D3)=-58.5 E(D1,D2,D3)=-58.7	H	0.0003935060	1.0090222955	-1.7724994770
			H	0.2609873303	-1.3482916268	1.1494632907
			H	-0.3697756867	-0.8893485662	-1.9052899747
			S	0.4981237979	-0.1131821796	-1.2315483277
			Si	-0.3915017593	0.0288457448	1.0390615819
i1a: HSiSH ₂  T1 diagnostic: 0.01477086	163.46 225.90 432.76 436.28 722.54 1206.31 1997.86 2673.89 2679.92	E(D0)=-52.5 E(D1)=-53.8 E(D2)=-55.3 E(D3)=-55.3 E(D1,D2,D3)=-55.2	H	-0.0015617101	1.4809419224	1.2122198795
			H	0.9684244707	0.7933280396	-1.4670774062
			H	-0.9700785413	0.7912018574	-1.4669068765
			S	0.0001568099	-0.0785599453	-1.1402225695
			Si	0.0003314886	-0.0422403169	1.3297447969

i2: H ₂ SiSH  T1 diagnostic: 0.01852358	233.70 513.08 553.07 682.20 812.49 913.13 2184.91 2229.17 2698.40	E(D0)=-215.8 E(D1)=-217.8 E(D2)=-218.3 E(D3)=-217.8 E(D1,D2,D3)=-218.3	H -0.0725257577 1.2400496850 -1.7198885632 H 0.1391215870 -1.2863381361 1.1445888941 H -0.2081773596 -1.1918438291 -1.8938658389 S -0.2467688427 -0.0247930143 0.8992717405 Si 0.3865775612 -0.0500290377 -1.1509191393
i3: H ₃ SiS  T1 diagnostic: 0.01299818	429.05 495.46 560.88 920.45 922.13 972.38 2228.05 2245.06 2247.13	E(D0)=-215.4 E(D1)=-217.8 E(D2)=-217.8 E(D3)=-217.8 E(D1,D2,D3)=-218.5	H -0.7053306888 1.2064166061 -1.6057582649 H -0.7055177224 -1.2064663757 -1.6057202364 H 1.3978469431 0.0001254761 -1.5012968320 S 0.0476275678 -0.0000044712 1.0530729633 Si -0.0251973911 -0.0000712355 -1.0877839074
TS: i1a – i1b  T1 diagnostic: 0.01454585	167.91 i 220.82 418.86 457.26 716.51 1202.10 2003.06 2676.95 2711.73	E(D0)=-51.0 E(D1)=-53.8 E(D2)=-52.1 E(D3)=-53.8 E(D1,D2,D3)=-53.5	H -0.0123311133 -1.0289923027 -1.7210828235 H -0.4036145457 -1.3040386741 0.9045779622 H -0.4252254333 0.8680813375 -1.7419544033 S 0.5915338944 0.0987905737 -1.3200351844 Si 0.2478643861 0.0532047334 1.1576815421
TS: i1a – i2  T1 diagnostic: 0.01908338	704.89 i 349.94 402.62 536.41 744.64 930.92 1414.00 2043.09 2706.86	E(D0)=-23.9 E(D1)=-26.7 E(D2)=-24.1 E(D3)=-25.5 E(D1,D2,D3)=-24.2	H 1.0761229146 -0.1720676996 -0.9023103276 H -0.7688441944 -0.6486134386 -0.0888945962 H 0.8694153546 -0.7814042028 1.5894413571 S -0.0347175877 0.5575801979 -0.7267120551 Si -0.4993555372 -0.1230668568 1.5775944418
TS: i1b – i2  T1 diagnostic: 0.01915692	665.39 i 351.03 480.76 523.13 837.38 1039.69 1458.06 2039.71 2694.48	E(D0)=-30.3 E(D1)=-31.9 E(D2)=-33.3 E(D3)=-30.8 E(D1,D2,D3)=-31.1	H -0.1581234079 1.1760144278 -1.7294475338 H 0.2362076436 -1.4070535429 0.8917866757 H -0.5435573903 -0.8584828748 -0.8698758097 S -0.3825350130 -0.2739811602 0.5255274234 Si 0.8462353561 0.0505488177 -1.5388036623

TS: i1a – SiSH  T1 diagnostic: 0.01532170	1174.19 i 332.28 361.24 618.28 987.42 1091.37 1453.78 1766.31 2674.03	E(D0)=-3.3 E(D1)=-6.0 E(D2)=-3.8 E(D3)=-4.9 E(D1,D2,D3)=-3.7	H -0.1627126861 0.4575626717 -2.0988434848 H 0.2137768879 -0.9266738266 -0.4886360802 H -0.3351369496 -1.4120897042 0.2937734088 S 0.8257018958 0.4269246957 -1.1896799672 Si -0.5434019598 0.1413218312 0.7625732166
TS: i1b – t-HSiSH  T1 diagnostic: 0.02953411	816.29 i 208.83 365.75 496.51 609.96 708.31 916.52 2051.05 2695.95	E(D0)=23.1 E(D1)=19.9 E(D2)=21.3 E(D3)=25.9 E(D1,D2,D3)=25.1	H -0.0016860697 0.9876538231 -1.5372396614 H 0.3354538983 -1.2327832020 1.3619182647 H -0.5264501878 -1.0174605390 -2.5129845076 S 0.4616446767 -0.1586981065 -1.0186298335 Si -0.2707351293 0.1083336920 0.9861228309
TS: i1a – c-HSiSH  T1 diagnostic: 0.02930655	835.11 i 224.29 345.35 485.56 585.34 715.16 801.20 2046.20 2705.70	E(D0)=33.7 E(D1)=32.0 E(D2)=30.7 E(D3)=36.5 E(D1,D2,D3)=35.9	H 0.2645467141 -1.2028860774 1.4591198480 H 0.8308947216 -1.1168827663 -1.0001363218 H 2.0303767102 0.7203788712 -1.5495965466 S 0.2557350098 0.0912969574 -0.9377358263 Si -0.3630780658 0.1421572551 1.1388969768
TS: i2 – i3  T1 diagnostic: 0.01427596	1341.90 i 515.82 566.72 595.20 628.29 930.80 1710.96 2235.65 2263.05	E(D0)=-119.9 E(D1)=-122.0 E(D2)=-122.0 E(D3)=-119.9 E(D1,D2,D3)=-120.0	H -0.8280755407 1.2332114783 -1.7675479778 H -0.8367543593 -1.2335779015 -1.7580963620 H 1.3454283731 -0.0037506674 -0.6965108041 S 0.5398447628 0.0044872355 0.7156201412 Si -0.2110145273 -0.0003701452 -1.2409512748
TS: i2 – SiSH  T1 diagnostic: 0.03228793	1212.81 i 388.72 477.73 500.79 662.48 836.70 1591.31 1691.91 2685.50	E(D0)=-34.2 E(D1)=-34.8 E(D2)=-37.0 E(D3)=-34.3 E(D1,D2,D3)=-33.5	H -0.2389002069 0.7887057229 -1.6180597204 H 0.3179559118 -1.0120199990 1.4521525533 H -0.3719666851 -0.4954450728 -2.1705816973 S -0.4747746828 -0.2376083375 0.6941427583 Si 0.7659128513 -0.3565866458 -1.0784668007

 TS: i2 – H ₂ SiS T1 diagnostic: 0.02249936	560.50 i 126.59 195.81 610.61 611.15 701.52 996.69 2241.15 2257.05	E(D0)=-36.3 E(D1)=-33.2 E(D2)=-38.5 E(D3)=-38.5 E(D1,D2,D3)=-33.3	H -0.0031480161 -1.9327522017 1.9285719718 H 1.2150637956 -0.1015826553 -1.8482330848 H -1.2155844270 -0.0977248266 -1.8474330501 S 0.0004609955 0.0988763472 0.9482859326 Si 0.0001085382 -0.0201381253 -1.0106728362
 TS: i3 – HSiS T1 diagnostic: 0.02758986	972.79 i 438.88 510.13 675.63 879.78 958.69 1519.46 1928.36 2287.49	E(D0)=-45.6 E(D1)=-46.3 E(D2)=-47.9 E(D3)=-46.7 E(D1,D2,D3)=-45.3	H 0.0134612112 1.0221655240 -1.7044330334 H -0.8773267545 -1.1131920597 -1.6882748693 H 0.8748438347 0.5007529830 -1.7582971504 S -0.0025648348 -0.0334602251 1.1721801991 Si 0.0010152520 -0.3762662225 -0.7686614234
 H ₂ T1 diagnostic: 0.00601239	4400.22		H 0.0000000000 0.0000000000 0.3715191784 H 0.0000000000 0.0000000000 -0.3715191784
 HSiS T1 diagnostic: 0.03565980	577.18 692.59 2029.11	E(HSiS+H ₂)=-133.9 E(DSiS+H ₂)=-134.8 E(HSiS+HD)=-134.0 E(DSiS+D ₂)=-131.3	H 0.0000000000 1.2374246601 -1.7921712477 S 0.0000000000 0.0106422259 0.9596721427 Si 0.0000000000 -0.0512338506 -1.0060931678
 SiSH T1 diagnostic: 0.01827924	510.32 667.54 2630.06	E(SiSH+H ₂)=-114.5 E(SiSD+H ₂)=-116.6 E(SiSH+HD)=-114.6 E(SiSD+D ₂)=-113.1	H 0.0000000000 1.1799831517 -1.5695610837 S 0.0000000000 -0.1125267945 -1.1904889181 Si 0.0000000000 0.1293766784 0.9214577290
 H ₂ SiS T1 diagnostic: 0.01747638	614.44 636.23 717.46 1005.81 2236.96 2249.80	E(D0)=-42.3 E(D1)=-44.4 E(D2)=-44.4 E(D1,D2)=-38.7	H -0.0022686497 1.2202515430 -1.8556186086 H 0.0054933914 -1.2015802377 -1.8408225640 S -0.0048384390 0.0264361371 0.9542773806 Si -0.0003070689 0.0145171489 -0.9990731088
 t-HSiSH T1 diagnostic: 0.01672500	516.99 626.36 634.15 912.17 2048.92 2683.39	E(D0)=6.0 E(D1)=3.0 E(D2)=4.2 E(D1,D2)=9.1	H -1.1009437415 0.0000000000 2.4062455267 H 1.2741902382 0.0000000000 -0.3788405158 S 0.1788465601 0.0000000000 1.9996623518 Si -0.2184420568 0.0000000000 -0.0951663628

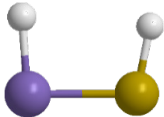
 <p>c-HSiSH</p> <p>T1 diagnostic: 0.01699851</p>	507.66	E(D0)=15.7	H	-0.0000960212	1.2924313596	-1.2088926370
	536.78	E(D1)=13.0	H	0.0004095851	1.4406316565	1.3034694552
	662.19	E(D2)=14.1	S	-0.0003580214	-0.0310749324	-0.9922990305
	807.13	E(D1,D2)=19.1	Si	0.0000265565	-0.0702965394	1.1528746985
	2045.24					
	2696.53					

Table S2. Physical parameters adopted for the Orion sources.

	Orion Hot Core	Orion Plateau	Orion 15.5 km s ⁻¹ component
n(H ₂) cm ⁻³	5 × 10 ⁷	10 ⁶	5 × 10 ⁶
T (K)	225	125	200
N(H ₂) cm ⁻²	4.2 × 10 ²³	2.1 × 10 ²³	10 ²³

Table S3. D and D₂ loss product mass combinations of silicon and sulfur isotopes from the reaction of ground state atomic silicon (Si(³P)) and deuterium sulfide (D₂S; X¹A₁). Isotope abundance given in parenthesis.

Si + D ₂ S		D ₂ ³² S (94.93%) 36	D ₂ ³³ S (0.76%) 37	D ₂ ³⁴ S (4.29%) 38	D ₂ ³⁶ S (0.02%) 40
D Loss	²⁸ Si (92.23%) 28	²⁸ Si ³² SD 62	²⁸ Si ³³ SD 63	²⁸ Si ³⁴ SD 64	²⁸ Si ³⁶ SD 66
	²⁹ Si (4.68%) 29	²⁹ Si ³² SD 63	²⁹ Si ³³ SD 64	²⁹ Si ³⁴ SD 65	²⁹ Si ³⁶ SD 67
	³⁰ Si (3.09%) 30	³⁰ Si ³² SD 64	³⁰ Si ³³ SD 65	³⁰ Si ³⁴ SD 66	³⁰ Si ³⁶ SD 68
D ₂ Loss	²⁸ Si (92.23%) 28	²⁸ Si ³² S 60	²⁸ Si ³³ S 61	²⁸ Si ³⁴ S 62	²⁸ Si ³⁶ S 64
	²⁹ Si (4.68%) 29	²⁹ Si ³² S 61	²⁹ Si ³³ S 62	²⁹ Si ³⁴ S 63	²⁹ Si ³⁶ S 65
	³⁰ Si (3.09%) 30	³⁰ Si ³² S 62	³⁰ Si ³³ S 63	³⁰ Si ³⁴ S 64	³⁰ Si ³⁶ S 66

Table S4. H and H₂ loss product mass combinations of silicon and sulfur isotopes from the reaction of ground state atomic silicon (Si(³P)) and hydrogen sulfide (H₂S; X¹A₁). Isotope abundance given in parenthesis.

Si + H ₂ S		H ₂ ³² S (94.93%) 34	H ₂ ³³ S (0.76%) 35	H ₂ ³⁴ S (4.29%) 36	H ₂ ³⁶ S (0.02%) 38
H Loss	²⁸ Si (92.23%) 28	²⁸ Si ³² SH 61	²⁸ Si ³³ SH 62	²⁸ Si ³⁴ SH 63	²⁸ Si ³⁶ SH 65
	²⁹ Si (4.68%) 29	²⁹ Si ³² SH 62	²⁹ Si ³³ SH 63	²⁹ Si ³⁴ SH 64	²⁹ Si ³⁶ SH 66
	³⁰ Si (3.09%) 30	³⁰ Si ³² SH 63	³⁰ Si ³³ SH 64	³⁰ Si ³⁴ SH 65	³⁰ Si ³⁶ SH 67
H ₂ Loss	²⁸ Si (92.23%) 28	²⁸ Si ³² S 60	²⁸ Si ³³ S 61	²⁸ Si ³⁴ S 62	²⁸ Si ³⁶ S 64
	²⁹ Si (4.68%) 29	²⁹ Si ³² S 61	²⁹ Si ³³ S 62	²⁹ Si ³⁴ S 63	²⁹ Si ³⁶ S 65
	³⁰ Si (3.09%) 30	³⁰ Si ³² S 62	³⁰ Si ³³ S 63	³⁰ Si ³⁴ S 64	³⁰ Si ³⁶ S 66

Table S5. D and D₂ loss product mass combinations of silicon and sulfur isotopes from the reaction of the D1-silyldiyne radical (SiD; X²Π) and deuterium sulfide (D₂S; X¹A₁). Isotope abundance given in parenthesis.

SiD + D ₂ S		D ₂ ³² S (94.93%) 36	D ₂ ³³ S (0.76%) 37	D ₂ ³⁴ S (4.29%) 38	D ₂ ³⁶ S (0.02%) 40
D Loss	²⁸ SiD (92.23%) 30	²⁸ Si ³² SD ₂ 64	²⁸ Si ³³ SD ₂ 65	²⁸ Si ³⁴ SD ₂ 66	²⁸ Si ³⁶ SD ₂ 68
	²⁹ SiD (4.68%) 31	²⁹ Si ³² SD ₂ 65	²⁹ Si ³³ SD ₂ 66	²⁹ Si ³⁴ SD ₂ 67	²⁹ Si ³⁶ SD ₂ 69
	³⁰ SiD (3.09%) 32	³⁰ Si ³² SD ₂ 66	³⁰ Si ³³ SD ₂ 67	³⁰ Si ³⁴ SD ₂ 68	³⁰ Si ³⁶ SD ₂ 70
D ₂ Loss	²⁸ SiD (92.23%) 30	²⁸ Si ³² SD 62	²⁸ Si ³³ SD 63	²⁸ Si ³⁴ SD 64	²⁸ Si ³⁶ SD 66
	²⁹ SiD (4.68%) 31	²⁹ Si ³² SD 63	²⁹ Si ³³ SD 64	²⁹ Si ³⁴ SD 65	²⁹ Si ³⁶ SD 67
	³⁰ SiD (3.09%) 32	³⁰ Si ³² SD 64	³⁰ Si ³³ SD 65	³⁰ Si ³⁴ SD 66	³⁰ Si ³⁶ SD 68

Table S6. H, D, H₂, and HD loss product mass combinations of silicon and sulfur isotopes from the reaction of the D1-silyldyne radical (SiD; X²Π) and hydrogen sulfide (H₂S; X¹A₁). Isotope abundance given in parenthesis.

SiD + H ₂ S		H ₂ ³² S (94.93%) 34	H ₂ ³³ S (0.76%) 35	H ₂ ³⁴ S (4.29%) 36	H ₂ ³⁶ S (0.02%) 38
H Loss	²⁸ SiD (92.23%) 30	²⁸ Si ³² SHD 63	²⁸ Si ³³ SHD 64	²⁸ Si ³⁴ SHD 65	²⁸ Si ³⁶ SHD 67
	²⁹ SiD (4.68%) 31	²⁹ Si ³² SHD 64	²⁹ Si ³³ SHD 65	²⁹ Si ³⁴ SHD 66	²⁹ Si ³⁶ SHD 68
	³⁰ SiD (3.09%) 32	³⁰ Si ³² SHD 65	³⁰ Si ³³ SHD 66	³⁰ Si ³⁴ SHD 67	³⁰ Si ³⁶ SHD 69
D Loss	²⁸ SiD (92.23%) 30	²⁸ Si ³² SH ₂ 62	²⁸ Si ³³ SH ₂ 63	²⁸ Si ³⁴ SH ₂ 64	²⁸ Si ³⁶ SH ₂ 66
	²⁹ SiD (4.68%) 31	²⁹ Si ³² SH ₂ 63	²⁹ Si ³³ SH ₂ 64	²⁹ Si ³⁴ SH ₂ 65	²⁹ Si ³⁶ SH ₂ 67
	³⁰ SiD (3.09%) 32	³⁰ Si ³² SH ₂ 64	³⁰ Si ³³ SH ₂ 65	³⁰ Si ³⁴ SH ₂ 66	³⁰ Si ³⁶ SH ₂ 68
H ₂ Loss	²⁸ SiD (92.23%) 30	²⁸ Si ³² SD 62	²⁸ Si ³³ SD 63	²⁸ Si ³⁴ SD 64	²⁸ Si ³⁶ SD 66
	²⁹ SiD (4.68%) 31	²⁹ Si ³² SD 63	²⁹ Si ³³ SD 64	²⁹ Si ³⁴ SD 65	²⁹ Si ³⁶ SD 67
	³⁰ SiD (3.09%) 32	³⁰ Si ³² SD 64	³⁰ Si ³³ SD 65	³⁰ Si ³⁴ SD 66	³⁰ Si ³⁶ SD 68
HD Loss	²⁸ SiD (92.23%) 30	²⁸ Si ³² SH 61	²⁸ Si ³³ SH 62	²⁸ Si ³⁴ SH 63	²⁸ Si ³⁶ SH 65
	²⁹ SiD (4.68%) 31	²⁹ Si ³² SH 62	²⁹ Si ³³ SH 63	²⁹ Si ³⁴ SH 64	²⁹ Si ³⁶ SH 66
	³⁰ SiD (3.09%) 32	³⁰ Si ³² SH 63	³⁰ Si ³³ SH 64	³⁰ Si ³⁴ SH 65	³⁰ Si ³⁶ SH 67

Table S7. Fractional abundance ranges for SiS in the Orion Sources shown in Figure 13.

Source	Light Grey	Dark Grey	Light Grey
Orion Hot Core	$(1.8\text{--}5.4) \times 10^{-10}$	$(5.4\text{--}8.8) \times 10^{-10}$	$(8.8\text{--}26.4) \times 10^{-10}$
Orion Plateau	$(0.43\text{--}1.29) \times 10^{-9}$	$(1.29\text{--}2.05) \times 10^{-9}$	$(2.05\text{--}6.14) \times 10^{-9}$
Orion 15.5 km s ⁻¹	$(1.76\text{--}5.3) \times 10^{-9}$	$(5.3\text{--}8.7) \times 10^{-9}$	$(8.7\text{--}26.1) \times 10^{-9}$

References

1. D. Proch and T. Trickl, *Review of Scientific Instruments*, 1989, **60**, 713-716.
2. T. Shiozaki, G. Knizia and H.-J. Werner, *The Journal of Chemical Physics*, 2011, **134**, 034113.